Journal of Rock Mechanics and Geotechnical Engineering 18 (2026) 3571–3588

Contents lists available at ScienceDirect

Journal of Rock Mechanics and Geotechnical Engineering

journal homepage: www.jrmge.cn

Full Length Article

# Effects of cylindrical-obstacle spacing on granular shock wave interactions in gravity-driven flows

Zheng Chen [a,*], Jian Wang [a], Dongpo Wang [a], Siming He [b,c,**]

[a] State Key Laboratory of Geohazard Prevention and Geoenvironment Protection, Chengdu University of Technology, Chengdu, 610059, China
[b] Institute of Mountain Hazards and Environment, Chinese Academy of Sciences, Chengdu, 610299, China
[c] University of Chinese Academy of Sciences, Beijing, 100049, China

ARTICLE INFO

*Article history:*
Received 14 January 2025
Received in revised form
9 October 2025
Accepted 30 October 2025
Available online 28 January 2026

*Keywords:*
Granular flow
Cylindrical obstacles
Shock waves
Impact pressures

ABSTRACT

Hazardous geophysical granular flows, such as debris flows and rock avalanches, can exert intense impact forces on obstacles and threaten downstream structures located in their paths. Installing protective structures can mitigate damage, but quantifying their influence on flow evolution and impact loading remains challenging. This study investigates the interactions of granular shock waves (GSWs) generated in front of two cylindrical obstacles with varying spacings through chute experiments and discrete element modeling. Impact pressure sensors were mounted on the upstream surface of each cylinder and on the chute bed to measure dynamic impact pressures in the GSW region. Granular flow velocity and depth were obtained using image processing. Results demonstrate that cylinder spacing significantly influences the geometric characteristics of GSWs. Runup increases with steady-state Froude number ($Fr_{steady}$) but decreases as spacing narrows. The granular vacuum length grows with bed slope but decreases significantly with decreasing cylinder spacing. Impact pressures on the cylinders and the chute bed increase linearly with $Fr_{steady}$. Low-frequency power spectral density (PSD) is positively correlated with $Fr_{steady}$, whereas centroid frequency and pressure impulse counts exhibit low sensitivity to $Fr_{steady}$. The dimensionless impact pressure coefficient ($\alpha$) decreases nonlinearly with increasing Froude number ($Fr$). At low $Fr$, $\alpha$ values for dry granular flows are lower than those for debris flows, but the difference diminishes at higher $Fr$. These findings may improve our understanding of granular flow–obstacle interactions and might help to design protective structures.



## 1. Introduction

Hazardous geophysical granular flows, such as rock avalanches, debris flows, and landslides, frequently occur in mountainous regions, driven downslope by gravity (Fischer et al., 2012). Some high-velocity mass flows can exert intense impact forces on obstacles, causing significant damage to structures such as buildings, bridges, dams, and railways along their paths (Armanini, 2007; Jakob et al., 2012; Zhu et al., 2020). To mitigate the damage caused by these granular free-surface flow hazards, passive defense and regulation technologies have been developed, designed to protect the objects by altering or intercepting granular flow trajectories. The typical protective measures include flexible barriers (Kwan et al., 2014; Song et al., 2018), dams (Shieh et al., 2008; Shen et al., 2019), and defensive barrier systems (Bi et al., 2018; Chen et al., 2022). For a defensive system consisting of multiple structures, one of the critical challenges is quantifying the dynamic processes involved in granular flows impacting multiple structures and the dynamic interaction between the granular shock waves (GSWs). The characteristics of GSWs are closely related to the shape and size of the defense structures, as well as the spacing distance between them (Khan et al., 2020; Chen et al., 2021, 2022).

Previous studies have investigated the formation of GSWs around obstacles, highlighting a pivotal role in defining the granular flow dynamics (Gray and Cui, 2007; Pudasaini and Kröner, 2008; Johnson and Gray, 2011; Cui and Gray, 2013). These

* Corresponding author.
** Corresponding author. Institute of Mountain Hazards and Environment, Chinese Academy of Sciences, Chengdu, 610299, China.
*E-mail addresses:* zheng.chen@cdut.edu.cn (Z. Chen), hsm@imde.ac.cn (S. He).

Peer review under responsibility of Institute of Rock and Soil Mechanics, Chinese Academy of Sciences.

https://doi.org/10.1016/j.jrmge.2025.10.034

studies have emphasized the dynamic interactions between granular flows and obstacles, focusing particularly on the GSWs that arise immediately upstream of obstacles, where substantial variations in flow depth and velocity are observed (Tai et al., 2001; Gray et al., 2003; Heil et al., 2004; Cui and Gray, 2013; Iverson et al., 2016). Additionally, granular shock dynamics have been analyzed through stationary granular jumps, analogous to hydraulic jumps in open channels (Savage, 1979; Brennen et al., 1983). Experimental investigations have further examined GSWs by employing various obstacle forms, such as retention dams (Faug et al., 2008), rigid walls (Faug, 2015a; Pudasaini et al., 2007; Pudasaini and Kröner, 2008), flat or inclined surfaces (Boudet et al., 2007; Iverson et al., 2016), wedges (Gray et al., 2003), and circular obstacles (Boudet and Kellay, 2010; Cui and Gray, 2013; Heil et al., 2004; Chen et al., 2021). These studies have advanced our understanding of granular flow dynamics, particularly through laboratory analyses involving cylindrical structures (Boudet and Kellay, 2010; Cui and Gray, 2013) and comprehensive dynamic models that account for the complex obstacle shapes and configurations (Kattel et al., 2018; Kafle et al., 2019; Chen et al., 2022; Jaiswal et al., 2023; Pudasaini et al., 2024).

However, significant challenges remain in understanding the kinematic evolution of rapid granular flows interacting with defense systems consisting of multiple structures, mainly due to the instability of granular flows, complex fluid–structure interactions, and potential structural damage (Kang and Kim, 2016; Dai et al., 2017; Wang et al., 2018a). Of particular importance is how the granular flow evolves and interacts with the structures after being disturbed by upstream defenses, as this directly influences the extent of the downstream protective region. Quantifying the runup height of the granular flows on the structures is also essential for designing effective defenses to prevent overtopping.

Dynamic impact forces and pressures are key factors for understanding the interactions between granular flows and protective structures (Albaba et al., 2017; Calvetti et al., 2017; Wang et al., 2018b). They are also essential for characterizing particle behavior within shock-affected regions and for guiding the design of protective structures (Chen et al., 2021, 2022). Extensive research based on laboratory flume experiments and field observations has significantly contributed to developing dynamic models for estimating the forces and pressures exerted by granular flows (Scotton and Deganutti, 1997; Zanuttigh and Lamberti, 2006; Tiberghien et al., 2007; Hübl et al., 2009; Moriguchi et al., 2009; Chen et al., 2010; Armanini et al., 2011; Hu et al., 2011; Bugnion et al., 2012; Cui et al., 2015; Wendeler and Volkwein, 2015; Vagnon and Segalini, 2016; Wang et al., 2018a, 2018b; Zhang et al., 2024a). Furthermore, the mechanisms of impact and energy dissipation during granular flows–obstacle interactions have been studied through flume experiments (Scheidl et al., 2013; Choi et al., 2014; Ng et al., 2017).

Numerical simulations provide a powerful complementary tool for investigating the properties of granular flows and earth surface processes (Pudasaini et al., 2005; George and Iverson, 2014; Liang et al., 2019). These methods are invaluable for validating experimental data and exploring scenarios that are difficult to reproduce physically (Albaba et al., 2017; Calvetti et al., 2017). Various numerical algorithms, including the discrete element method (DEM), smoothed particle hydrodynamics (SPH), material point method (MPM), finite difference method (FDM), and finite volume method (FVM), have been employed to simulate the evolution of gravity-driven single-phase and multiphase geophysical flows such as landslides, debris flows, and debris floods. Among these approaches, DEM stands out for its ability to capture microscale inter-particle interactions (Zhang et al., 2024b), which are challenging to observe in physical experiments. In this study, we employ DEM modeling to analyze inter-particle forces and collision mechanisms in granular shocks.

Despite considerable research on GSWs, limited attention has been paid to the interactions between granular shocks generated by structures arranged at different spacings. Several key questions remain, such as how granular shocks interact and evolve, as well as how the underlying mechanisms of these interactions can be quantitatively described. This study aims to address these gaps through small-scale laboratory experiments, focusing on the geometric features and the dynamic impact pressures of granular flows applied to two circular cylinders with different spacings. Additionally, DEM simulations are conducted to analyze the evolution and dynamic responses of granular flow interacting with these cylinders, thereby providing detailed insight into particle collisions during shock-wave interactions. This research advances our understanding of GSW dynamics and offers valuable guidance for the design of protective structures.

## 2. Methods

### 2.1. Controlled experiment

#### 2.1.1. Experimental set-up

The controlled granular flow experiments were conducted in 2019 using an indoor experimental chute facility in Chengdu, China (Chen et al., 2021). The chute facility can be delineated into four functional zones: the initiation hopper, the chute channel, the impact plate (with two cylinders fixed on the plate), and the collection box (see Fig. 1a). This chute facility, constructed from plexiglass, extends over a length of 2500 mm and a width of 800 mm, positioned at an angle $\theta$ relative to the horizontal plane, adjustable via a hydraulic mechanism. A gate mechanism at the hopper, measuring 100 mm in height, regulates the influx of granular material into the chute. Two identical cylinders are anchored into pre-drilled holes on an interchangeable plate fixed to the chute bed, positioned 1220 mm downstream from the hopper outlet. The center-to-center spacing between the holes is denoted as $D$, which is varied by replacing the plate, as illustrated in Fig. 1b and c. Fabricated from hollow aluminum, these cylindrical obstacles each have a radius of $R_c = 60$ mm, a height of 280 mm, and a wall thickness of 10 mm. A circular aperture, 27 mm in diameter, is precision-drilled into the surface of each obstacle, situated 23.5 mm above the chute bed, to accommodate a pressure sensor. The coordinate system is established with the $x$-axis oriented in the direction of descent, the $y$-axis aligned laterally across the slope, and the $z$-axis pointing up, perpendicular to the bed of the chute.

The measurement devices consisted of two cameras and four dynamic pressure sensors, which were used during the laboratory experiments to record flow velocity, flow depth, and dynamic impact pressures of the granular flows. The entire process of granular flow impacting the cylindrical obstacles was captured by the two cameras, which were placed directly above and on the side of the chute. The cameras operated at a maximum resolution of 3840 $\times$ 2160 pixels and at a maximum frame rate of 240 fps at 1920 $\times$ 1080 pixels resolution. Tape colored in black affixed to the chute sidewalls provided a reference scale for measuring flow depth, while yellow tape attached to the chute bed and cylinder surfaces was used to determine flow velocity and runup height, respectively. A pressure sensor (C) was screwed in each cylinder, with its sensing surface flush with the cylinder surface and its center positioned 23.5 mm above the chute bed. Two additional pressure sensors (B) were embedded in the chute bed immediately upstream of each cylinder, with their surfaces flush with the chute bed. Thus, the pressure sensors C were utilized to measure the

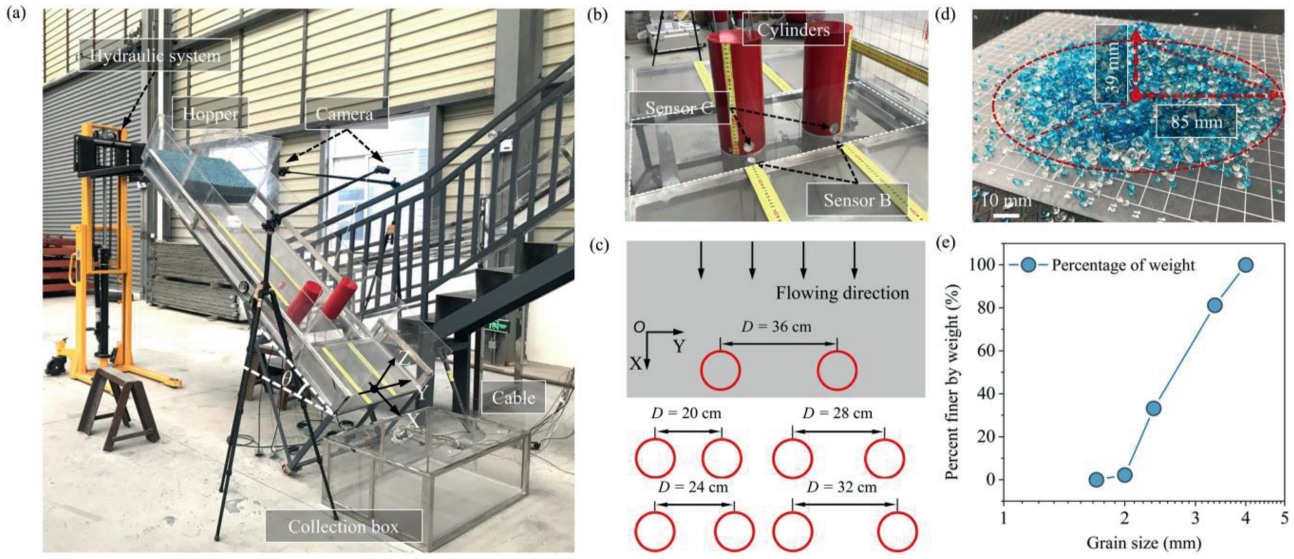


**Fig. 1.** Indoor granular flow experiment facility. (a) The experimental chute consists of the initiation hopper shown in transparent color, the flowing channel (with scale marks on its side walls), the impact plate with two cylinders, and the collection box. (b) The impact pressure sensors (B on the bed and C on the cylinders) recording the dynamic impact pressures generated by granular flows impacting on the chute bed and the cylinders. (c) Arrangement of the two cylinders fixed on a plate flush with the chute bed, with the cylinder center located 780 mm upstream from the chute outlet. (d) Experimental granular materials. A sandpile test was performed on a plate with a 1 cm × 1 cm grid, producing a pile about 170 mm in diameter and 39 mm in height. (e) Grain size distribution of the particles used in the experiments.

dynamic impact pressure generated on the surface of the cylinder in the *x*-direction, while the sensors B recorded the impact pressures on the chute bed in the *z*-direction (Fig. 1b). The impact pressure sensors (model CYG17127) were custom-manufactured for this study. Each sensor has a surface area of 572.6 $mm^2$ and a measurement range of 0–200 kPa. During the experiments, all sensors are connected to a data-acquisition system operating at a sampling frequency of 2000 Hz.

For all experimental runs, the gate opening height and the *x*-positions of the two cylinders remained constant, while the spacing distance $D$ was varied. The experiments were therefore controlled by the inclination angle $\theta$ of the chute bed and the spacing distance $D$ between the two cylinders, with $\theta$ changing from 30° to 38° and $D$ from 20 cm to 36 cm (Fig. 1c). After loading the mixed granular material into the hopper at the top of the chute without intentional layering, the gate was opened, releasing the particles into the chute. The granular flow then moved downslope, driven by gravity, impacted the cylinders, and was eventually collected in the box at the chute outlet.

### 2.1.2. Granular material

The granular mixture (comprising blue and white glass beads; see Fig. 1d) was thoroughly mixed prior to each experiment to ensure a homogeneous initial condition. The grain size distribution (GSD; 1.7–4 mm; Fig. 1e) was relatively narrow and remained constant across all experimental runs. For each experiment, the glass–bead mixture has a constant GSD and a fixed released mass of 100 kg. The bulk density of the glass–bead mixture was determined to be 1646 kg/$m^3$, while the internal friction angle and the friction angle with the chute bed were approximately 24.6° and 20°, respectively (Chen et al., 2021). The chute sidewalls were assumed to be smooth, and wall friction effects were considered negligible owing to their sufficient distance from the cylinders.

## 2.2. Granular shock characterization

### 2.2.1. Runup

Predicting the runup height of hazardous geophysical granular flows is of practical significance for the design of protective structures, as excessive runup can cause overtopping of barriers or engineering structures located along the flow path (Hungr et al., 1984). Furthermore, runup heights observed on topographic obstacles have been used to estimate the minimum flow velocity of gravity-driven mass flows, by assuming a balance between kinetic energy and gravitational potential energy (e.g. Jibson et al., 2006). Typically, four runup models of debris flows were summarized by Iverson et al. (2016):

(1) Frictionless point mass model: $h_2 = 0.5g/u_1^2$, where $h_2$ is the runup height, $u_1$ is the incoming flow velocity, and $g$ is the gravitational acceleration.
(2) Frictionless finite mass model: $h_2/h_1 = u_1^2/(gh_1) + 1$, where $h_1$ is the incoming flow depth.
(3) Momentum jump model: $h_2/h_1 = [2u_1^2/(kgh_1)]\left\{(h_2/h_1)/\left[(h_2/h_1)^2 - 1\right]\right\} + 1$, where $k$ is the earth pressure coefficient.
(4) Smooth momentum flux model: $h_2/h_1 = [u_1^2/(gh_1)][1 + gh_1 k\cos^3\theta/(2u_1^2)](1 + \tan\phi/\tan\theta)$, where $\theta$ is the slope angle, and $\phi$ is the effective basal friction angle between the debris flow and slope.

All four models assume that the flow is uniform, steady, and one-dimensional, and moves along a horizontal or inclined plane. Model 1 treats debris flow as a frictionless point mass, assuming that all initial kinetic energy is converted into gravitational potential energy during vertical runup against an obstacle. Model 2 accounts for the gravitational potential energy of a finite-thickness flow, assuming that total energy is converted into the potential energy of the center of mass. Model 3 incorporates sudden momentum changes (e.g. shocks or jumps) and assumes constant flow density before and after impact. Model 4 considers a smooth mass and momentum transfer from the flow body to the flow head during runup against a slope, assuming equal densities for the incoming flow and the mass flowing on the slope. In this

framework, all energy dissipation occurs within the shock, whereas the smooth transfer model attributes dissipation to basal friction.

If a debris flow overtops an obstacle during the impact process, forming a hydraulic jump-like phenomenon, a separate model is required to describe the jump height. For a frictionless flow moving along a plane, the runup height can be predicted using the hydraulic jump model, which is derived from the depth-averaged mass and momentum conservation equations with the source terms neglected:

$$h_1\overline{u_1}=h_2\overline{u_2} \tag{1}$$

$$h_1(\overline{u_1})^2+\frac{1}{2}gh_1^2\cos\theta=h_2(\overline{u_2})^2+\frac{1}{2}gh_2^2\cos\theta \tag{2}$$

where $\overline{u_1}$ and $\overline{u_2}$ are the depth-averaged flow velocity before and after an impact, respectively. By substituting Eq. (1) into Eq. (2), we obtained:

$$\frac{h_2}{h_1}=\frac{1}{2}\left(\sqrt{1+8Fr^2}-1\right) \tag{3}$$

where $Fr$ is the Froude number, a widely used dimensionless parameter that represents the ratio of inertial to gravitational forces in gravity-driven flows. The classic form of the Froude number is expressed as $Fr=\overline{u}/\sqrt{gh\cos\theta}$.

In this study, when the steady-state flow velocity $\overline{u_s}$ and flow depth $\overline{h_s}$ of the incoming flow are measured, the dimensionless runup height $h_2^*$ can be expressed as: $h_2^*=h_2/\overline{h_s}=\frac{1}{2}\left(\sqrt{1+8Fr_{steady}^2}-1\right)$, where $Fr_{steady}=\overline{u_s}/\sqrt{g\overline{h_s}\cos\theta}$ is the Froude number of granular flow at steady state. To identify the steady-state stage, the entire granular impact process is divided into three parts: the flow front head, the steady flow body, and the tail. The steady stage corresponds to the period when the main body of the granular flow interacts with the obstacles, during which both velocity and depth remain relatively constant, as illustrated in Fig. 3. The values of $\overline{u_s}$ and $\overline{h_s}$ used to calculate $Fr_{steady}$ are measured at a location approximately 4 cm upstream of the cylinders, outside the granular shock influence zone, to ensure that the measurements reflect the undisturbed incoming flow conditions.

Furthermore, based on the hydraulic jump model, Faug (2015b) proposed a formulation to calculate the granular flow runup height, expressed as

$$\frac{h_2}{h_1}=\frac{1}{2}\left(\sqrt{1+8\chi Fr^2}-1\right) \tag{4}$$

where $\chi=\lambda/\left[k-KL(\tan\theta-\mu_b)(h_2-h_1)^{-1}\right]$ is the tuning parameter that links classical hydraulic jumps ($\chi=1$) to granular jumps; the parameter $\beta$ represents the velocity-profile shape coefficient of the granular flow, which is assumed to be linear ($\lambda=1$) in this study; $L$ is the length of granular jump region, which is taken as $L=10h_1$; and $K$ is the shape-related coefficient of the jump. Generally, if the value of $L/h_1$ is not considerably large, the influence of $K$ is weak, and thus $K=1$ is adopted (Chen et al., 2021). The basal friction coefficient $\mu_b$ and the earth pressure coefficient $k$ are typically treated as functions of the internal and basal friction angles, as suggested by Savage and Hutter (1989), and can be derived from classical soil mechanics principles. In this study, since the impact pressures in both the $x$- and $z$-directions were measured, $k$ can also be determined experimentally using the following equation:

$$k=\frac{\sigma_{xx}}{\sigma_{zz}}=\frac{IMP_{mean\_body,C}}{IMP_{mean\_body,B}} \tag{5}$$

where $\sigma_{xx}$ and $\sigma_{zz}$ indicate the stress in the $x$- and $z$-directions, respectively; $IMP_{mean\_body,C}$ and $IMP_{mean\_body,B}$ are the mean impact pressures generated by granular flow body on the cylinder and chute bed, respectively, as defined in Section 2.3.2.

#### 2.2.2. Granular shock interactions

The released granular particles flowing downslope along the chute are interfered by the two cylinders, diverting around both sides of each cylinder. The velocity and depth of the granular flow are significantly altered, resulting in the formation of two bow-shaped shock waves. On the lee side of each cylinder, a particle-free zone forms, commonly referred to as the granular vacuum, as shown in Fig. 2b. The two shock waves separate from each cylinder in the form of a parabolic crest and interact intensely near the central region. As a result, the shape of the shock waves along the channel sizes differs from that in the central region. Fig. 2c summarizes geometric characteristics of the GSWs, including the standoff distance ($D_{standoff}$) and the pinch-off distance of the granular vacuum ($D_{pinch\text{-}off}$), referring to the definition proposed by Cui and Gray (2013). Based on overhead view images captured by the camera positioned above the chute bed during the steady-state stage of the flow, $D_{standoff}$ and $D_{pinch\text{-}off}$ were calculated by proportional scaling following the image processing method proposed by Chen et al. (2021). Specifically, the dimensionless spacing $D^*$ is defined based on the net gap between the two cylinders, calculated as $D^*=(D-2R_c)/2R_c$, where $D$ is the center-to-center distance and $R_c$ is the cylinder radius. In this study, both $D_{standoff}$ and $D_{pinch\text{-}off}$ are normalized by the cylinder diameter ($2R_c$).

#### 2.2.3. Measurement of the velocity

The average surface velocity $\overline{u}$ and the flow depth $h$ of the granular flow were measured at $x=1100$ mm downstream from the hopper gate, while the two cylinders were located at $x=1220$ mm. Given the temporal and spatial fluctuations of $\overline{u}$ and $h$ , this study focuses on the flow front velocity, $\overline{u}_{front}$, measured just before the granular flow reaches the cylinders. The value of $h$ is obtained according to the flow images recorded by the camera in the side view, by reading the ruler value on the transparent side wall of the chute. The value of $\overline{u}_{front}$ was calculated from the image frames before particle–cylinder collisions using the image processing method according to Chen et al. (2021). For $\overline{u}_{steady}$, 20 consecutive frames of images were selected after the experimental flow reached a steady state to minimize the random fluctuations in the measurements. The video frames were processed using the PIVLab package (Thielicke and Sonntag, 2021) to obtain the spatial velocity fields.

#### 2.2.4. Depth-averaged velocity

Gravity-driven free-surface granular flows can be effectively described using depth-averaged mass and momentum conservation equations (Pudasaini and Krautblatter, 2022). The application of classical shallow flow assumptions to granular flows, as introduced by Savage and Hutter (1989), has advanced the mathematical modeling of natural hazards such as landslides, avalanches, and debris flows. This approach assumes that the vertical scale (flow depth, $h$) is much smaller compared to the slope length ($L$), i.e. $h/L\ll1$, which is widely applicable to various geophysical granular flows. Given the shallow depth and the relatively small velocity variation within the granular layers compared to the basal sliding velocity in this experiment, a plug

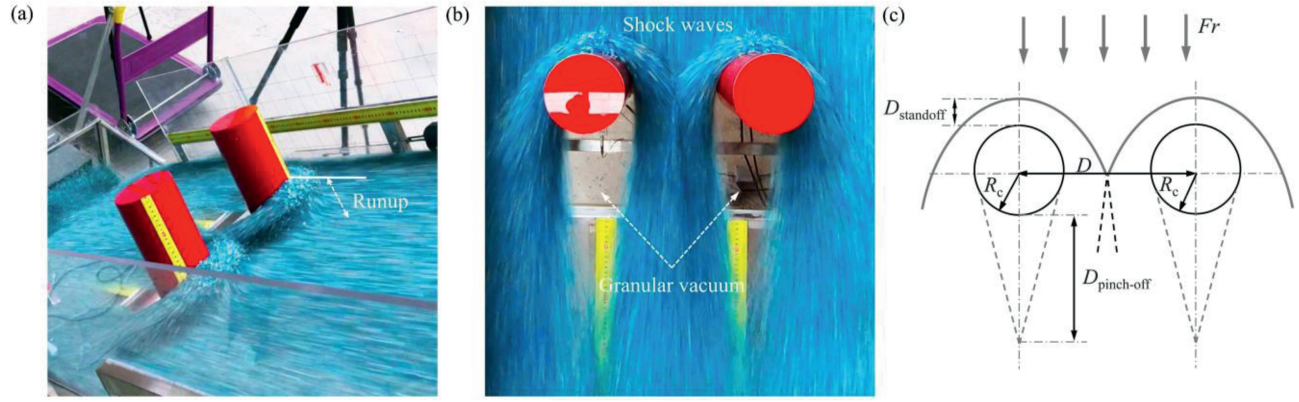


**Fig. 2.** (a) Perspective view of two GSWs generated as granular flow impacts and flows around two circular cylinders; (b) The overhead views showing the fully developed GSWs upstream of the two cylinders and the particle-free region (granular vacuum) formed on the lee side of the cylinders; and (c) Geometric characteristics of the interaction between the two GSWs extracted from panel (b).

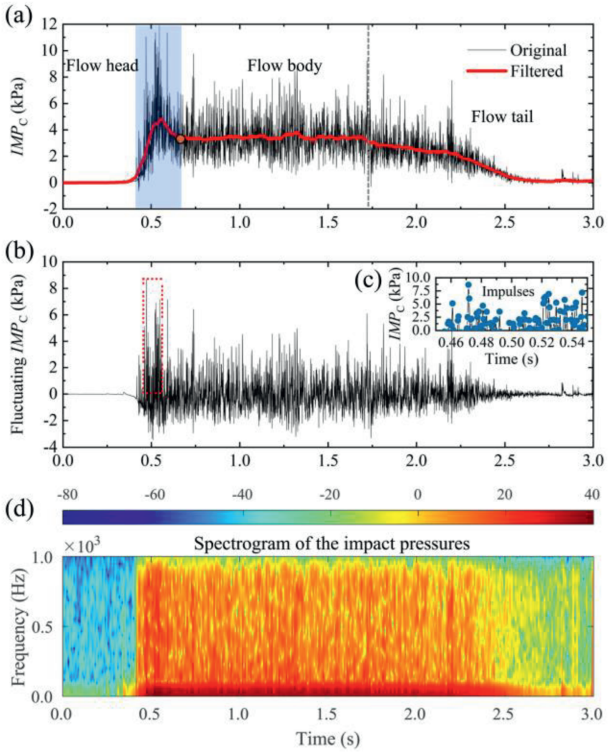


**Fig. 3.** Illustration of the impact pressures generated on one of the two cylinders. (a) The entire impact process is divided into three phases: the head, body, and tail of the granular flow, respectively. The impact pressures are recorded by the pressure sensor C with $D = 20$ cm and a slope angle of $\theta = 34°$. The light black line and thick red line represent the original and filtered (low-frequency component) impact pressures, respectively. (b) The fluctuating (high-frequency component) pressure signals obtained by subtracting the low-frequency signal from the original signals, with the blue dots representing impulses generated by single particle impacts (c). (d) Spectrogram of the original impact pressures.

flow condition is assumed, under which the surface velocity is approximately equal to the depth-averaged velocity. Under steady-state conditions ($\partial h/\partial t \approx 0$), the transverse velocity $\bar{v}$ is much smaller than the downslope velocity $\bar{u}$ of the granular flow, thus assuming $\bar{v} = 0$. Consequently, the depth-averaged equations for one-dimensional free-surface granular flow down an inclined chute at an angle $\theta$ can be expressed as (Gray et al., 2003; Cui and Gray, 2013; Cui et al., 2022):

$$\frac{\partial}{\partial x}(h\bar{u}) = 0 \tag{6}$$

$$\frac{\partial}{\partial x}\left(h\bar{u}^2 + \frac{1}{2}gh^2\cos\theta\right) = (\tan\theta - \mu_b)gh\cos\theta \tag{7}$$

where $\mu_b$ is the basal friction coefficient. The $x$-axis points downslope, the $y$-axis points across the slope, and the $z$-axis points vertically upward, perpendicular to the bed.

Eq. (6) can be directly integrated with appropriate boundary conditions. For a known flow velocity $\overline{u_0}$ and flow depth $h_0$ at a position $x = x_0$ in the flow field, we obtain $h\bar{u} = h_0\overline{u_0}$. Substituting Eq. (6) into Eq. (7) yields a simplified form: $\bar{u}\frac{\partial\bar{u}}{\partial x} + g\cos\theta\frac{\partial h}{\partial x} = (\tan\theta - \mu_b)g\cos\theta$. Integrating this simplified equation and substituting $h = h_0\overline{u_0}/u$ leads to a polynomial expression for the flow velocity, denoted as Eq. (8). Numerical solutions of Eq. (8) produce three real roots, two of which are positive and correspond to accelerating and decelerating downslope flows (Cui and Gray, 2013), respectively. More sophisticated depth-averaged formulations and analytical velocity solutions have since been developed to better describe complex granular flow behaviors such as landslides and debris flows (Pudasaini, 2011, 2024; Pudasaini and Krautblatter, 2022).

$$\bar{u}^3 - \left[2g\cos\theta(\tan\theta - \mu_b)(x - x_0) + \overline{u_0}^2 + 2gh_0\cos\theta\right]\bar{u} + 2gh_0\overline{u_0}\cos\theta = 0 \tag{8}$$

### 2.3. Impact pressure processing

#### 2.3.1. Impact pressure filtering

The typical impact pressures recorded during a granular flow experiment are presented in Fig. 3a, exhibiting numerous impact-induced impulses. Previous studies on debris flow have revealed that the smooth components of the pressure signals arise from continuous and uniform fluid pressure, whereas peak impulses result from individual large particles (Hu et al., 2011). The smooth signals triggered by debris flow have been extracted using the wavelet analysis (Cui et al., 2015). In this study, the Daubechies wavelet is used to analyze and decompose the granular flow impact pressure signals. Specifically, the Daubechies (db4) wavelet is chosen as the basis wavelet function, and the original signal is decomposed into 8 levels using the discrete wavelet transform:

$$f(t) = A_8(t) + \sum_{i=1}^{8} D_i(t) \tag{9}$$

where $A_8(t)$ represents a smooth, low-frequency component of the signal reconstructed from the approximate coefficients $c_{8,k}$ and the scaling functions $\phi_{8,k}(t)$, i.e. $A_8(t) = \sum_k c_{8,k}\phi_{8,k}(t)$. Each $D_i(t)$ represents the high-frequency detail component at level $i$, reconstructed from the detail coefficients $d_{i,k}$ and the wavelet functions $\psi_{i,k}(t)$, i.e. $D_i(t) = \sum_k d_{i,k}\psi_{i,k}(t)$. The 8th-level approximation component is used to reconstruct the smoothed impact pressures, while the fluctuating (high-frequency) pressures are then obtained by subtracting the reconstructed smooth signal from the original signal (Fig. 3).

#### 2.3.2. Impact pressure characteristics

(1) Amplitude

The dynamic impact pressures generated by granular flow on obstacles can be divided into three stages: a sudden and intense impact caused by the granular flow head, a sustained impact caused by the granular flow body, and a weak impact caused by the granular flow tail (Chen et al., 2021). This division is based on the statistical analysis of experimental pressure signals. Specifically, the flow head phase is defined from the moment of the initial pressure rise to the point (see the orange dot in Fig. 3a), where it drops after reaching the peak. This turning point marks the transition from the relatively short head impact to the more stable impact of the granular flow body. In our experiments, the flow head phase consistently lasted approximately 0.2 s, the flow body phase approximately 1 s, and the remaining pressure decay is attributed to the flow tail. These durations were determined across all tests with a total impact process of about 2 s. Our segmentation method is conceptually similar to the approach proposed by Cui et al. (2015), who simplified the debris flow impact process into a combination of two impulsive forms (two triangles), representing the debris flow head and the continuous flow body impact. In their model, the debris flow head generates the peak dynamic pressure, followed by a sustained triangular-shaped body impact phase.

Based on the above definitions, we calculate the following variables to characterize the impact pressure generated by flow head and flow body: $IMP_{\text{peak\_head,C}}$, $IMP_{\text{mean\_head,C}}$, $IMP_{\text{peak\_body,C}}$, and $IMP_{\text{mean\_body,C}}$ from the pressure sensor C (mounted on the cylinder, see Fig. 1b) on the cylinder and $IMP_{\text{peak\_head,B}}$, $IMP_{\text{mean\_head,B}}$, $IMP_{\text{peak\_body,B}}$, and $IMP_{\text{mean\_body,B}}$ from the pressure sensor B (embedded in the chute bed) on the chute bed, respectively. $IMP_{\text{peak}}$ indicates the maximum impact pressures, which is calculated as the average of the 10 largest impact pressures, and $IMP_{\text{peak}} = \frac{1}{10}\sum_{k=1}^{10} IMP_{10,k}$, where $IMP_{10,k}$ is one of the 10 largest impact pressures triggered by granular flow during a test. $IMP_{\text{mean}}$ is the mean value of the effective impact pressures, which is calculated as $IMP_{\text{mean}} = \frac{1}{n}\sum_{k=1}^{n} IMP_{n,k}$, where $n$ is the total sampling numbers, and $IMP_{n,k}$ is the effective pressure impulse. In our experiment, the effective pressure means that $IMP_{n,k} \geq 20$ Pa. Variables related to the flow tail are not calculated as the impact during this stage is relatively weak and less important for engineering applications.

(2) Impulses

Following the definition of signal impulses generated by bedload particle transport (Rickenmann et al., 2014), we define the impulse $IMP(t)$ as an effective impact pressure whose amplitude exceeds a predefined threshold (20 Pa). As shown in Fig. 3c, the time intervals between adjacent peaks represent the duration of the collision between the particles and the pressure sensor. Generally, the impulse represents the oscillation process of the stress wave at the measuring station, and a single impact event may contain several to tens of impulse responses. However, in this study, due to the small sensing area of the pressure sensor, we assume that a single impulse represents one impact event. Therefore, the frequency of the impact pressure may also reflect the impact rate of the particles (Chen et al., 2025).

(3) Centroid frequency

The centroid frequency $f_{\text{centroid}}$ is often used to characterize the spectral features of the signal (Farin et al., 2018, 2019; Chen et al., 2021). We use the following formula to calculate $f_{\text{centroid}}$ of impact pressure signals $IMP(t)$:

$$f_{\text{centroid}} = \frac{\int_0^{+\infty} |\tilde{A_Z}(f)| f \mathrm{d}f}{\int_0^{+\infty} |\tilde{A_Z}(f)| \mathrm{d}f} \tag{10}$$

where $|\tilde{A_Z}(f)|$ is the absolute value of the amplitude spectrum of the pressures obtained by the fast Fourier transform (FFT).

### 2.4. DEM simulation

#### 2.4.1. Model set-up

The discrete element method (DEM) is one of the numerical simulation methods to solve problems involving discontinuous media, which is widely used in simulating the motion and impact processes of discrete particles. In DEM simulations, each particle within an object is modeled as an independent unit and simulated individually. The interactions between particles are explained by solving the motion equations, which control the translational and rotational movements of the particles within the computational system. In this study, the DEM was utilized to simulate the process of granular flow driven by gravity moving on the chute and impacting with two cylindrical obstacles.

A virtual model of the experiment chute was generated through computer-aided design (CAD), consisting of different components such as the hopper, channel, sidewalls, and cylindrical obstacles. The inclination slope angle of the chute ranged from 30° to 38°, and the center-to-center spacing $D$ between the two cylinders varied from 120 mm to 360 mm. In the hopper at the top of the chute, a total of 100 kg of particles (approximately 0.53 million particles) were generated and allowed to settle into a static state, replicating the initial conditions of the laboratory experiments. A similar particle GSD was established based on the experimental data. The particles were modeled as ellipsoids to reduce computational complexity, while maintaining consistency in the GSD with the experiments (see Fig. 1e). The hopper gate was set to the same location as in the laboratory set-up, with a constant opening height of 100 mm. After the gate opened, particles were released under gravity ($g = 9.81$ m/s$^2$) and accelerated downslope along the chute. To compare with laboratory experiments, dynamic impact pressures were recorded at the corresponding positions of the cylinders and the chute bed. Output data were saved every 0.0005 s, equivalent to a sampling frequency of 2000 Hz. In addition, the velocity and depth of the granular flow were also recorded. The numerical time step was set to 20 % of the Rayleigh time step (approximately $1.44 \times 10^{-6}$ s) to ensure numerical stability. Tables A1 and A2 in Appendix A summarize the parameters of the materials and simulation settings used in the DEM simulations.

*2.4.2. Contact model*

The Hertz-Mindlin (no-slip) contact model is adopted to achieve accurate and efficient force calculations. The normal component of the contact force is based on Hertz contact theory, while the tangential component is computed using the Mindlin-Deresiewicz method (Mindlin, 1949; Mindlin and Deresiewicz, 1953). The normal and tangential damping components are calculated using the restitution coefficient. Tangential friction force obeys Coulomb's friction law, and rolling friction is implemented using the contact-independent directional constant torque model (Sakaguchi et al., 1993). The normal force $F_n$ is expressed as

$$F_n = 4 \Big/ 3E^* \sqrt{R^*} \delta_n^{3/2} \tag{11}$$

where $E^*$ is the equivalent Young's modulus of the particle, and $E^* = E_i E_j / \left[ E_i \left(1 - \nu_j^2\right) + E_j \left(1 - \nu_i^2\right) \right]$, in which $E_i$ and $E_j$ denote the elastic moduli of particles $i$ and $j$, respectively, and $\nu_i$ and $\nu_j$ denote the Poisson's ratios of particles $i$ and $j$, respectively; $R^*$ is the equivalent radius of the particle, which can be calculated as $R^* = R_i R_j / \left(R_i + R_j\right)$, in which $R_i$ and $R_j$ are the radii of particles $i$ and $j$, respectively; and $\delta_n$ is the normal overlap between particles. The expression for the damping force $F_n^d$ is calculated as

$$F_n^d = -2\sqrt{5/6}\beta\sqrt{S_n m^*} v_n^{rel} \tag{12}$$

where $m^*$ is the equivalent mass of the particle, and $m^* = m_i m_j / \left(m_i + m_j\right)$, in which $m_i$ and $m_j$ are the masses of particles $i$ and $j$, respectively; $v_n^{rel}$ is the normal component of the relative velocity between particles; the parameter $\beta = \ln e / \sqrt{\ln^2 e + \pi^2}$ is a function of the restitution coefficient $e$; and $S_n = 2E^* \sqrt{R^* \delta_n}$ is the normal stiffness.

The tangential force $F_t$ is determined by the tangential overlap $\delta_t$ and the tangential stiffness $S_t$:

$$F_t = -S_t \delta_t = -8\delta_t G^* \sqrt{R^* \delta_t} \tag{13}$$

where $G^*$ is the equivalent shear modulus of the particle, which is calculated as $G^* = G_i G_j / \left[ G_i \left(2 - \nu_j\right) + G_j (2 - \nu_i) \right]$, in which $G_i$ and $G_j$ are the shear moduli of particles $i$ and $j$, respectively, and $\nu_i$ and $\nu_j$ are the Poisson's ratios of particles $i$ and $j$, respectively. The tangential damping force $F_t^d$ is calculated using the following equation:

$$F_t^d = -2\sqrt{5/6}\beta\sqrt{S_t m^*} v_t^{rel} \tag{14}$$

where $v_t^{rel}$ is the tangential component of the relative velocity. The tangential force is determined as $\mu_s F_n$, where $\mu_s$ is the static friction coefficient. Additionally, rolling friction is represented by applying a torque on the contact surface, which can be expressed as

$$T_i = -\mu_r F_n R_i \omega_i \tag{15}$$

where $\mu_r$ is the rolling friction coefficient, $R_i$ is the distance from the contact point to the center of mass, and $\omega_i$ is the unit angular velocity vector at the contact point. The intrinsic parameters (e.g. density, shear modulus, and Poisson's ratio) for the particles, chute, and cylinders, as well as the contact parameters (restitution coefficient, static and rolling friction coefficients for particle–particle, particle–chute, and particle–cylinder interactions) employed in the DEM simulations, are provided in Appendix A.

## 3. Results

### 3.1. Time-dependent evolution of GSWs

A granular flow impacting on two cylinders in an overhead view is depicted in Fig. 4, indicating the formation and evolution of GSWs. Fig. 5 illustrates the corresponding temporal evolution simulated by the DEM modeling. In Figs. 4 and 5, the time interval between consecutive images is 0.3 s, with the cylinder spacing $D = 200$ mm and the slope angle of the chute bed $\theta = 32^\circ$. A visual difference in color contrast was noted at the flow front, where the leading edge appears lighter in blue, while the rear part was darker. This contrast is attributed to saltating particles at the granular flow front (Figs. 4a and 5a), resulting in a locally reduced flow thickness and bulk density. When particles collide with the cylinders, they rebound in a direction determined by the collision angle and are subsequently entrained downward by the undisturbed incoming granular flow. Separated parabolic shock waves form on each upstream cylinder, while a relatively long particle-free vacuum develops downstream of the cylinder (Figs. 4b and 5b), where a few moving particles are visible within the vacuum area. On the downstream side, particles are pushed inward by transverse pressure gradients on both sides, causing the boundaries of the two vacuum regions to intersect and close at sharp points further downstream (Figs. 4c and 5c). The length of the vacuum region contracts and reaches a steady state (Figs. 4d–f and 5d–f), with a scarce presence of particles within the vacuum area. During the steady-state stage of the granular flow, the morphology of the GSW region undergoes minimal changes. In the later stage of the granular flow, as the inflow mass decreases, the strength of the shock waves weakens (Figs. 4f and g, and 5f and g). Despite the simulations employing granular particles with different shapes compared to those used in the indoor experiments, the temporal evolution of the shock wave region in the simulations closely matches the observations made in the experiments throughout all stages of the granular flow.

### 3.2. Velocity of granular flow

Fig. 6 shows the surface flow velocity along the downslope ($x$-direction) under the configuration of dual-cylinder structure (CS-D), where the velocity was presented at the centerline of the chute ($y = 0.4$ m) and within the range of $0.4\ \text{m} \le x \le 1.2$ m. The results show that the granular flow velocity increases nonlinearly along the $x$-direction downslope. Since the two cylinders are located downstream at $x = 1.22$ m, their obstruction and the formation of shock waves disturb the local flow field.

In the DEM simulations, particles within a rectangular domain measuring 1200 mm in length ($x$-direction), 10 mm in width ($y$-direction), and 10 mm in height ($z$-direction), symmetrically centered along the chute midline ($y = 0.4$ m), were selected for analysis. At $t = 1.4$ s after gate release, the velocities of all particles in this domain were monitored (Fig. 6b), where each data point represents a particle velocity at its respective position. The results reveal that particle velocity fluctuates and increases nonlinearly with distance downslope ($x$), indicating an accelerating granular flow. Under the dual-cylinder configuration (CS-D), even without direct obstruction along the chute midline, a significant reduction in particle velocity is still observed. For instance, at an inclination angle of $\theta = 38^\circ$, the peak particle velocity decreases from approximately 2.8 m/s at $x = 1.05$ m to about 2 m/s at $x = 1.2$ m. This reduction is attributed to interactions between GSWs, as the

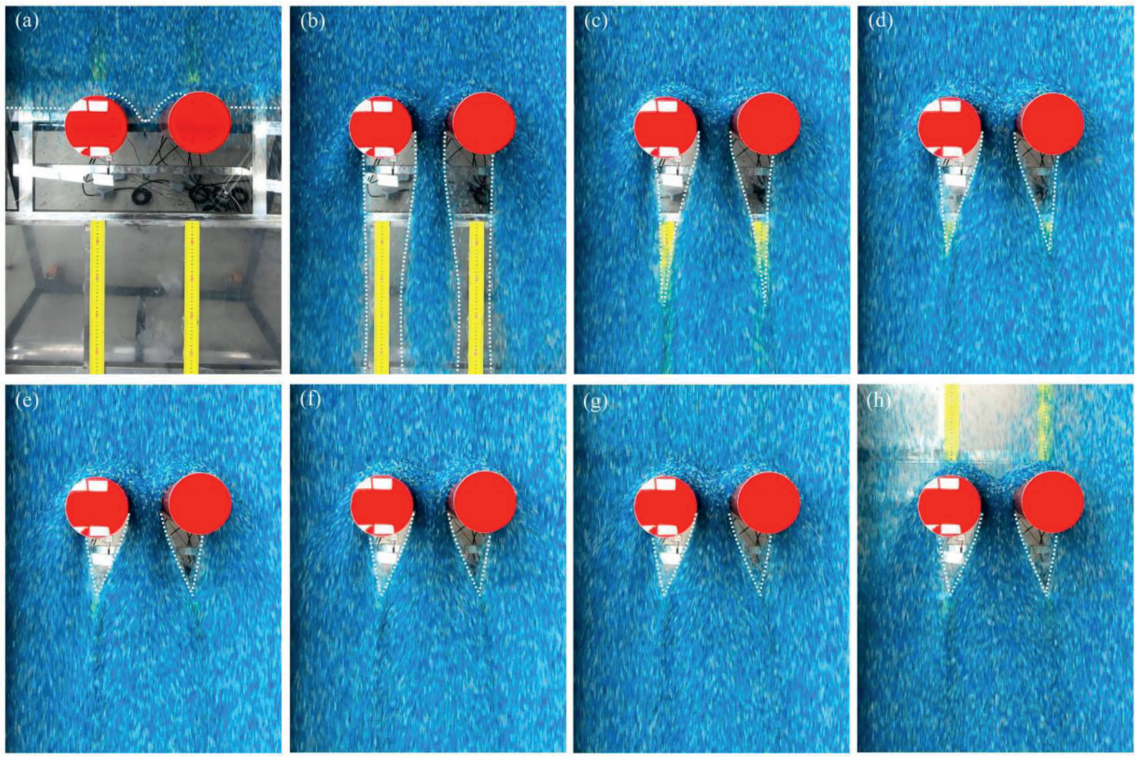


**Fig. 4.** Time-sequential overhead views of the granular flow impacting two cylinders in the laboratory experiment. The spacing distance between the two cylinders $D = 20$ cm, and the slope angle $\theta = 32°$. The time interval between consecutive images is 0.3 s.

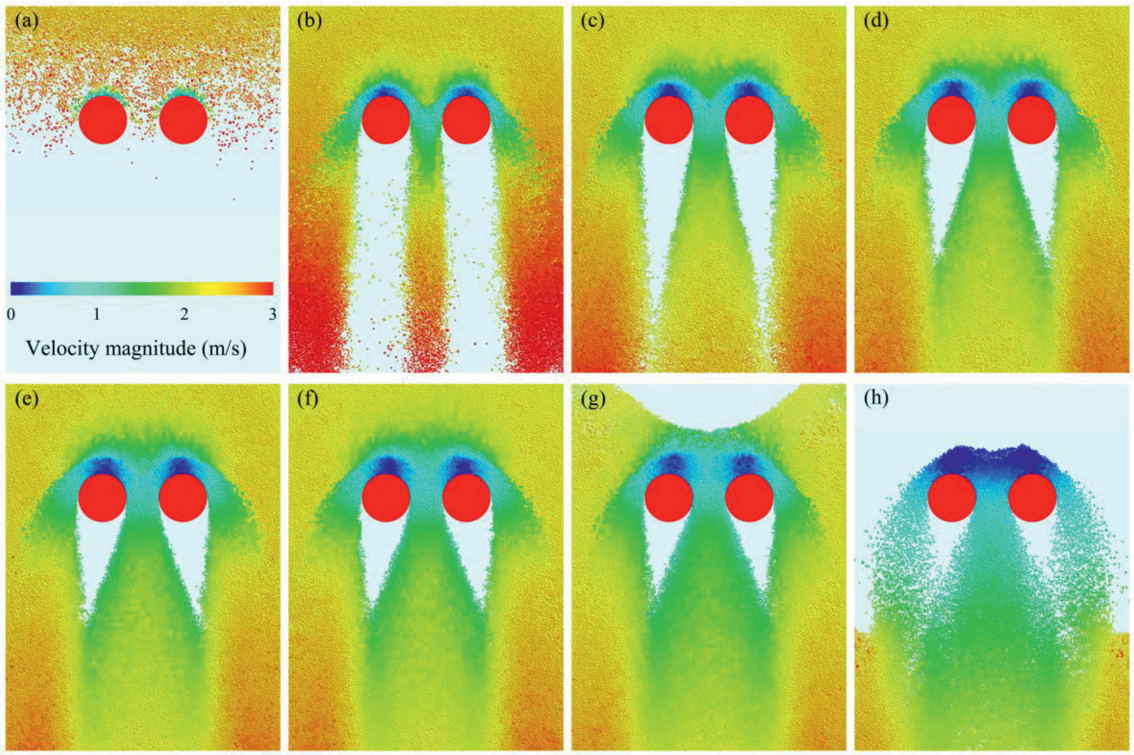


**Fig. 5.** Time-sequential overhead views of the granular flow impacting circular cylinders in DEM simulation. The spacing distance between the two cylinders $D = 20$ cm, and the slope angle $\theta = 32°$. The time interval between consecutive images is 0.3 s.

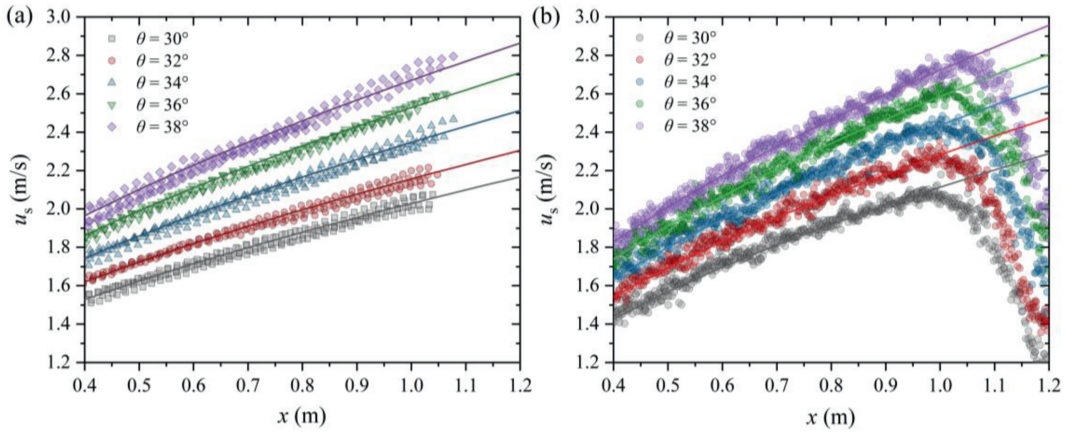


**Fig. 6.** Velocity distributions of granular flow along the chute downslope. (a) Experimental velocity distribution of granular flow in the *x*-direction for different chute bed slopes $\theta$ ranging from 30° to 38°. The velocity values were obtained during the steady state using image analysis, with the granular materials flowing from left to right along the inclined chute. (b) DEM simulation results of granular flow velocity distribution in the *x*-direction for the same range of chute slopes ($\theta = 30°$–38°). The solid lines indicate the theoretical velocities derived from the analytical analysis.

shocks generated by the two cylinders intersect along the centerline, where particle collisions are most intense.

Assuming a plug flow where the free-surface velocity equals the depth-averaged velocity, the flow velocity $\overline{u}$ along the downslope direction ($x$) has been described by Eq. (8). This equation can be reformulated as follows, using $\overline{u_0}$ and $h_0$ at $x = 1$ m:

$$x = \frac{1}{a_1}\left(\frac{\overline{u}^3 + c_1}{\overline{u}} - b_1\right) + 1 \tag{16}$$

where $a_1 = 2g\cos\theta(\tan\theta - \mu_b)$, $b_1 = 2gh_0\cos\theta + (\overline{u_0})^2$, and $c_1 = 2gh_0\overline{u_0}\cos\theta$.

For a given set of $\overline{u_0}$, $h_0$, and $\theta$, the calculated velocity can be fitted to the measured velocity by adjusting the basal friction coefficient $\mu_b$ until both velocity distributions $\overline{u}(x)$ coincide. Fitting was performed within the range $x = 0.4$–1 m, where the flow is fully developed, and the velocity field is not yet disturbed by the cylinders. This procedure allows for an accurate determination of the basal friction coefficient $\mu_b$ for the granular flow on the chute bed. Independent dynamic force balance test, based on basal impact pressures and particle acceleration (see Appendix B), indicates that $\mu_b$ ranges from 0.392 to 0.465 across different test conditions (average value ≈ 0.4), corresponding to a basal friction angle of 21.4°–24.9°. These values are slightly higher than the basal friction angle of 20° measured by the inclined plane tests. Two potential reasons may account for this difference: (1) free-surface velocity measurements may overestimate the actual depth-averaged velocity; (2) minor image distortion due to the camera not being perfectly perpendicular to the chute bed could affect velocity calibration, and (3) the underestimation of the basal impact pressures and particle acceleration (see Appendix B).

To further refine the friction coefficient used in theoretical analysis, the velocity distribution along the chute was fitted, as shown in the fitting $\overline{u}(x)$ curve in Fig. 6. The best-fit result was achieved by adjusting the friction coefficient $\mu_b$ to 0.36, corresponding to a basal friction angle of approximately 19.8°. This value provides a good agreement among the experimental measurements, DEM simulations, and theoretical predictions. This fitting-based friction coefficient is consistent with the inclined plane test result and is therefore adopted in subsequent analytical modeling and numerical simulations. These results also indicate that, under accurate velocity measurements, Eq. (8) effectively reflects the distribution of flow velocity along the *x*-direction and can be used to estimate the dynamic friction coefficient between the granular material and the chute bed.

### 3.3. Geometric properties of GSWs

Fig. 7 shows the experiment produced well-developed shock waves from around the cylinders with different spacing distances $D$ after reaching a steady state. The faint white stripes visible in the image frames trace the trajectories of the particles flowing around the two cylinders. Our observations reveal systematic variations in both the length of granular vacuum area (the pinch-off distance, $D_{\text{pinch-off}}$) and the standoff distance ($D_{\text{standoff}}$) as the cylinder spacing distances change, suggesting that the structural spacing affects the evolution of GSWs. For the large spacing distance ($D = 240$ mm; Fig. 7a), two independent shock waves are observed. The triangular vacuum regions on the lee side of the cylinders exhibit nearly straight boundaries, consistent with previous observations (Cui and Gray, 2013; Tregaskis et al., 2022). As the distance decreases, the two shock waves generated by the cylinders gradually interact near the central region. Particles diverted from the right cylinder deflect the flow wake leftward, while those from the left cylinder push the wake rightward, altering the shape of the granular vacuum region. The additional thrust causes an imbalance in the transverse pressure gradient on both sides of the granular vacuum, causing the side closer to the central region to bend inward, and reducing the area of the granular vacuum. For larger spacings, particles flow easily between the two cylinders, whereas smaller spacings generate greater resistance, leading to more intense particle interactions. The smallest granular vacuum area and the most curved boundaries are observed for $D = 80$ mm (see Fig. 7e). DEM simulation results in Fig. 7f–j exhibit similar characteristics in the evolution of the GSWs compared to the experimental results.

#### 3.3.1. Runup

Fig. 8a presents the runup height of granular flows impacting dual-cylinder structures (CS-D). Across all configurations, the runup height ($D_{\text{runup}}$) increases with the steady-state Froude number ($Fr_{\text{steady}}$), showing a rising trend as the dimensionless spacing ($D^*$) decreases. Comparisons with a single-cylinder structure (CS-S) from a prior granular flow experiment (Chen et al., 2021) reveal that for $D^* \leq 1$, the runup height of the granular flow for CS-D closely approached the runup height observed

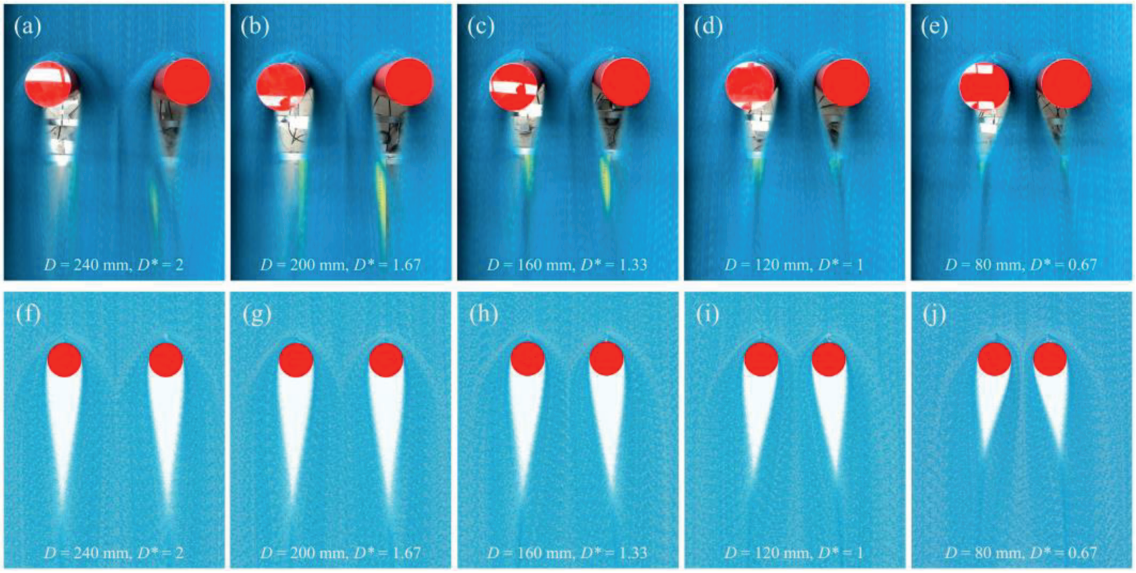


**Fig. 7.** (a–e) Photographs of steady-state GSWs observed in the experiments; and (f–j) Temporal evolution of simulated granular shock wave GSWs by DEM modeling. Both experimental and simulated results correspond to different cylinder spacing distances ranging from $D = 240$ mm to $D = 80$ mm and the slope angle $\theta = 32°$.

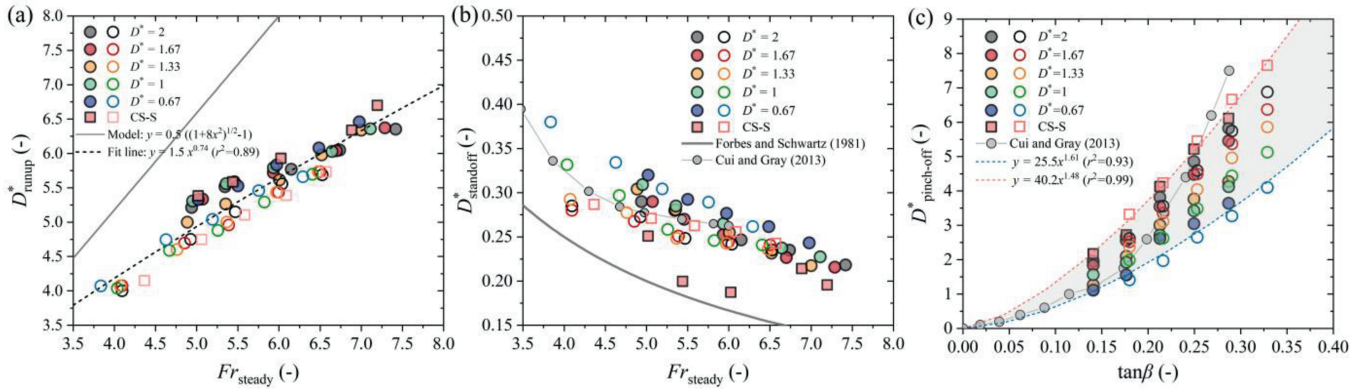


**Fig. 8.** Illustration of the geometric characteristics of GSWs generated on the two cylinders varying in spacing distances. (a) The dimensionless runup height ($D^*_{runup}$) as a function of the steady-state flow Froude number ($Fr_{steady}$). The dashed and solid lines represent the linear fits to the data and model predictions, respectively. (b) The relationship between the dimensionless standoff distance ($D^*_{standoff}$) and $Fr_{steady}$. (c) The functional relationship between the dimensionless pinch-off distance ($D^*_{pinch-off}$) and the net acceleration angle ($\beta$). Pink and blue dotted lines indicate the upper and lower bounds of the data in the present study, respectively. Filled and hollow symbols represent experimental and DEM simulation results, respectively.

for CS-S. When the cylinder spacing is further reduced to $D^* = 0.67$, the runup height in CS-D configurations surpasses that of the single-cylinder case, reaching a maximum runup height of 12.6 cm in our experiments. This trend is even more pronounced in DEM simulations, where the maximum runup height reached 13.3 cm for $D^* = 0.67$. In contrast, existing hydraulic jump models tend to overestimate the runup heights observed in both the experiments and DEM simulations.

### 3.3.2. Standoff distance

The relationship between the dimensionless standoff distance ($D^*_{standoff}$) of GSWs and $Fr_{steady}$ is presented in Fig. 8b. Experimental results indicate a nonlinear decrease in $D^*_{standoff}$ as $Fr_{steady}$ increases from approximately 5 to 7.5. The maximum observed $D^*_{standoff}$ of 0.32 occurs at a dimensionless spacing of $D^* = 0.67$. As the cylinder spacing increases, $D^*_{standoff}$ gradually decreases, and the differences among the experimental groups tend to reduce. These findings are consistent with the data reported by Cui and Gray (2013). DEM simulation results corroborate the experimental observations, especially at smaller spacings (e.g. $D^* = 0.67$), although slight discrepancies exist between the two datasets. These differences may arise because the experimental velocity was measured at the flow surface, whereas the flow is not perfectly plug-like and may have velocity gradients between granular layers. This could lead to an overestimation of the experimental Froude number $Fr_{steady\_exp}$ relative to the simulated value $Fr_{steady\_dem}$. Moreover, differences in particle shape and size between experiments and simulations may also have affected the $D^*_{standoff}$, particularly at narrow spacings.

### 3.3.3. Pinch-off distance

The dimensionless pinch-off distance ($D^*_{pinch-off}$) of the granular vacuums on the lee side of the cylinders is governed by the net acceleration angle ($\beta$). As $\beta$ approaches zero, $D^*_{pinch-off}$ diminishes to zero. In the present experiments, the base friction angle was

approximately 20°, combined with the chute slope ranging from 30° to 38°, resulting in $\beta$ between 10° and 18°. The experimental results, as depicted in Fig. 8c, indicate that for $D^* = 2$, where the interaction between two GSWs is relatively weak, $D^*_{\text{pinch-off}}$ ranges from 1.96 to 4.28 as tan$\beta$ increases. Beyond a slope angle of $\theta = 34°$ ($\beta = 14°$), the granular vacuum exceeds the channel range, precluding further data collection. As $D^*$ decreases from 2 to 0.67, the interaction between two shock waves becomes stronger, and the granular vacuum shape is disturbed by lateral flow, leading to a significant decrease in $D^*_{\text{pinch-off}}$. For $D^* = 0.67$, the minimum $D^*_{\text{pinch-off}}$ is 1.12, while $D^*_{\text{pinch-off}}$ reaches 3.64 at a slope angle of $\theta = 38°$ ($\beta = 18°$). The DEM simulations confirm this dependency, highlighting the sensitivity of $D^*_{\text{pinch-off}}$ to the dimensionless cylinder spacing ($D^*$).

### 3.4. Impact pressure signal characteristics

#### 3.4.1. Pressure amplitude

The peak and mean impact pressures ($IMP_{\text{peak\_head,C}}$, $IMP_{\text{mean\_head,C}}$, $IMP_{\text{peak\_head,B}}$, and $IMP_{\text{mean\_head,B}}$, recorded by pressure sensors (C and B) generated during the stage of flow head impacting on the cylinders, are shown as functions of the front flow Froude number $Fr_{\text{front}}$ (see Fig. 9a–d). We observed that both the peak ($IMP_{\text{peak\_head,C}}$ and $IMP_{\text{peak\_head,B}}$) and the mean impact pressures ($IMP_{\text{mean\_head,C}}$ and $IMP_{\text{mean\_head,B}}$) generated on the cylinders and the bed exhibit a linear increase with increasing $Fr_{\text{front}}$. Similarly, during the impact process generated by the granular flow body, the peak and mean impact pressures ($IMP_{\text{peak\_body,C}}$, $IMP_{\text{mean\_body,C}}$, $IMP_{\text{peak\_body,B}}$, and $IMP_{\text{mean\_body,B}}$) are shown as functions of the steady-state flow Froude number $Fr_{\text{steady}}$ in Fig. 10a–d, indicating also a linear relationship. In contrast, pressures generated during the flow tail stage are relatively weak and are less relevant for engineering applications (Chen et al., 2021). Therefore, we focus only on the flow head and body stages in this analysis. Across all impact stages, a dependency of impact pressures on the dimensionless cylinder spacing ($D^*$) is observed. Structural spacing has a greater influence on the impact pressures generated on the cylinder than on the chute bed. The results of the DEM data were presented in Fig. C1 in Appendix C and Fig. D1 in Appendix D, which demonstrate general agreement with the experimental data.

#### 3.4.2. Impulses

Both laboratory experiments and DEM simulations reveal that the impulse count of the fluctuating pressures ($N_{\text{impulse}}$), that is, the high-frequency component of the original impact pressures, shows only low sensitivity to $Fr_{\text{steady}}$ (Fig. 11a and b). A slight decreasing trend in $N_{\text{impulse}}$ with increasing $Fr_{\text{steady}}$ is observed in the experimental data, whereas the DEM simulations indicate nearly constant mean values. Specifically, the spacing between the cylinders ($D^*$) negatively affects $N_{\text{impulse}}$, with the highest impulse count observed at $D^* = 0.67$, which is likely due to enhanced particle–particle and particle–structure interactions.

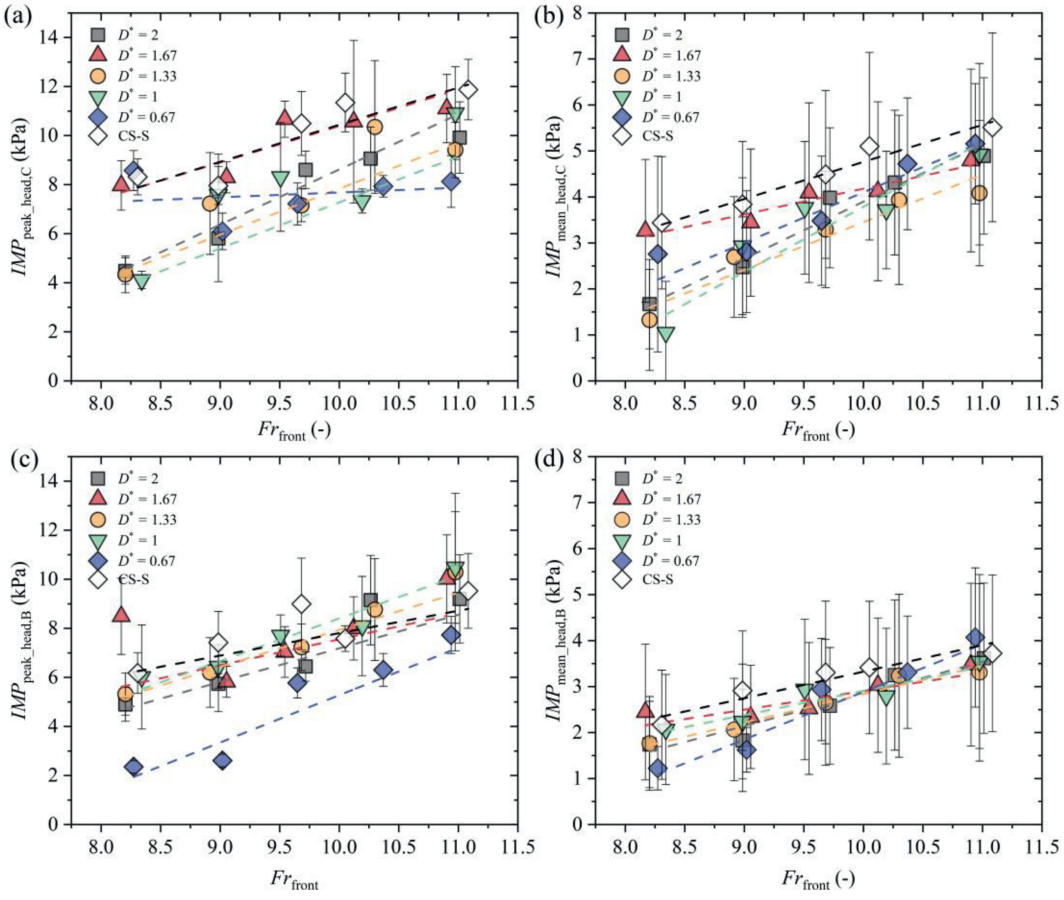


**Fig. 9.** Impact pressures generated during the granular flow head impact stage. (a, b) The peak ($IMP_{\text{peak\_head,C}}$) and mean ($IMP_{\text{mean\_head,C}}$) impact pressures on the cylinder surface as functions of the front flow Froude number ($Fr_{\text{front}}$), respectively; and (c, d) The corresponding peak ($IMP_{\text{peak\_head,B}}$) and mean ($IMP_{\text{mean\_head,B}}$) pressures generated by the granular flow on the chute bed as functions of $Fr_{\text{front}}$, respectively.

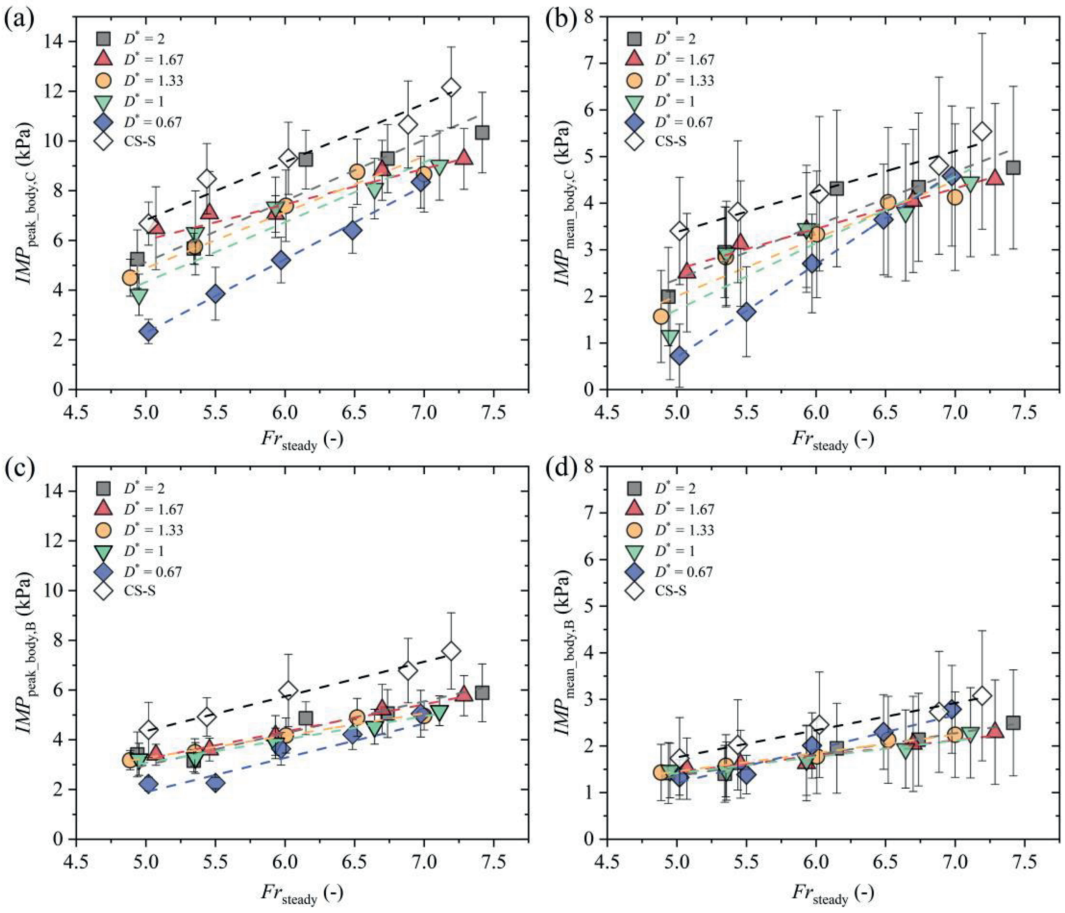


**Fig. 10.** Impact pressure generated during the granular flow body impact stage: (a, b) The peak ($IMP_{peak\_body,C}$) and mean ($IMP_{mean\_body,C}$) impact pressures generated on the cylinder surface as functions of steady-state flow Froude number $Fr_{steady}$, respectively; and (c, d) The corresponding peak ($IMP_{peak\_body,B}$) and mean ($IMP_{mean\_body,B}$) pressures on the chute bed as functions of $Fr_{steady}$, respectively.

### 3.4.3. Centroid frequency

The centroid frequency ($f_{centroid}$) of the fluctuating pressures generated by the granular flow body was analyzed using both experimental and DEM data. Fig. 11c and d illustrates the correlations between $f_{centroid}$ and $Fr_{steady}$ for impact pressures on the cylinder and on the chute bed. As $Fr_{steady}$ increases from approximately 4.8 to 7.4, $f_{centroid}$ fluctuates within a narrow range (around 30 Hz). Experimental impact pressures on the cylinders show that $f_{centroid}$ for CS-D configurations is generally lower than for CS-S, although the difference is not significant, reflecting the effects of reduced structural spacing on impact dynamics. Furthermore, both experimental and DEM results show that decreasing the cylinder spacing ($D^*$) tends to diminish the $f_{centroid}$ of the impact pressures on both the cylinders and the chute bed.

### 3.4.4. Power spectral density

We compared the low-frequency PSD ($P^0_{IMP}$) of the impact pressures generated by the granular flow body under different structural configurations, as shown in Fig. 12. Overall, $P^0_{IMP}$ demonstrates a positive nonlinear correlation with $Fr_{steady}$, reflecting increasing impact energy as flow intensity rises. For the cylinders (Fig. 12a), $P^0_{IMP}$ ranges from approximately $9.1 \times 10^{-4}$ kPa$^2$/Hz to $6 \times 10^{-3}$ kPa$^2$/Hz, while for the chute bed (Fig. 12b), it ranges from $3.7 \times 10^{-4}$ kPa$^2$/Hz to $2.3 \times 10^{-3}$ kPa$^2$/Hz. Notably, the cylinder-based $P^0_{IMP}$ values are approximately three times larger than those on the chute bed. Under the same flow condition, $P^0_{IMP}$ is higher for the single-cylinder configuration (CS-S) than the dual-cylinder configuration (CS-D). In contrast, the pressures measured on the chute bed without any obstacle influence are significantly weaker, with $P^0_{IMP}$ values ranging from $2.5 \times 10^{-5}$ kPa$^2$/Hz to $8.4 \times 10^{-5}$ kPa$^2$/Hz. This is one order of magnitude lower than the cylinder-based values in the CS-S configuration and corresponds to approximately 1/50–1/20 of the corresponding cylinder-based results. These observations underscore the significant influence of structures on the power of granular flow impact pressures, particularly on the chute bed.

DEM simulations corroborate these findings, demonstrating that $P^0_{IMP}$ increases with increasing $Fr_{steady}$ for both fluctuating pressures on the cylinders and the bed (Fig. 12). In the CS-S configuration, the $P^0_{IMP}$ values for the fluctuating pressures on the cylinder range from approximately $1.2 \times 10^{-3}$ kPa$^2$/Hz to $3.4 \times 10^{-3}$ kPa$^2$/Hz (Fig. 12a), whereas those on the chute bed range from approximately $3.1 \times 10^{-4}$ kPa$^2$/Hz to $7.9 \times 10^{-4}$ kPa$^2$/Hz (Fig. 12b), with $P^0_{IMP}$ values for cylinders being about 2.5 times higher. The consistency in the order of magnitude between experimental and simulation data highlights these findings. While $P^0_{IMP}$ values in simulations exhibit less sensitivity to changes in cylinder spacing, the overall trends align closely with experimental observations, reinforcing the impact of structural configurations on the power of impact pressures.

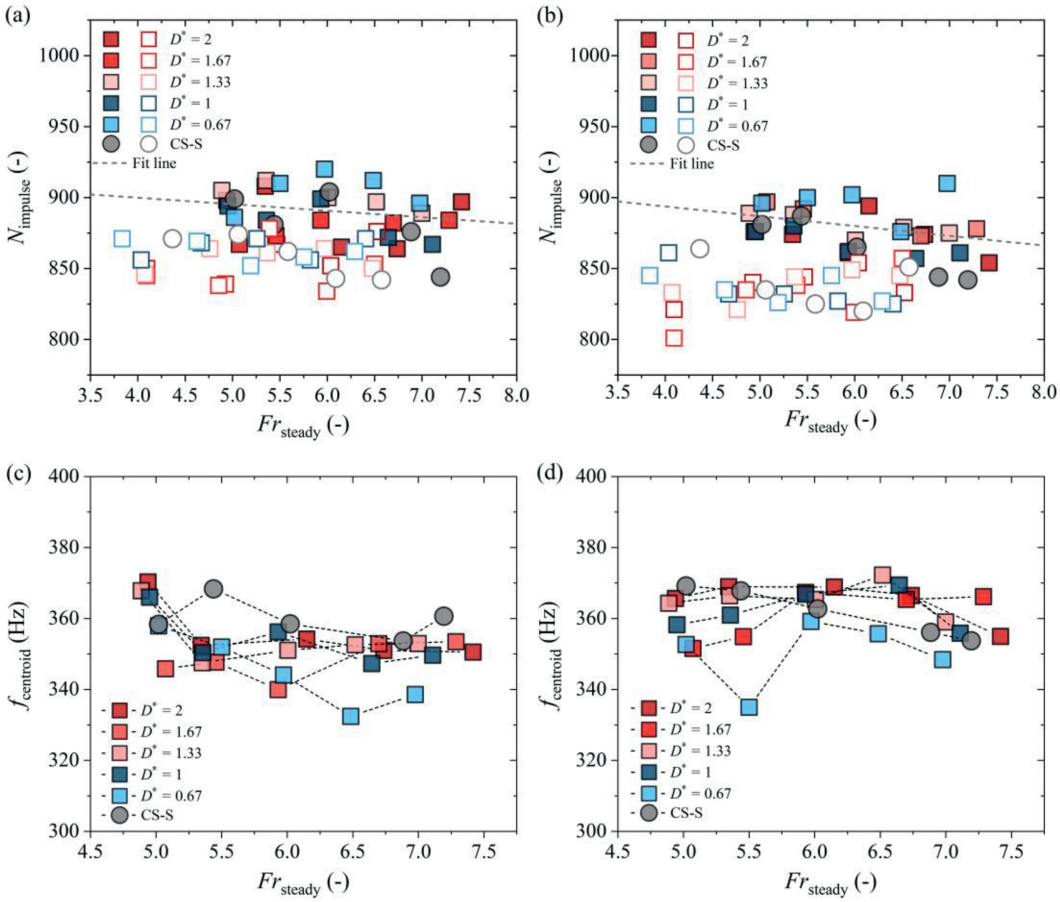


**Fig. 11.** Impulses and centroid frequency of the impact pressures as functions of the steady-state Froude number $Fr_{steady}$: (a) Impulse count ($N_{impulse}$) of the impact pressures generated by granular flow impacting on the cylinders with different spacing distances, based on experimental (solid dots) and DEM simulation (hollow dots) data; (b) $N_{impulse}$ for granular flow impacts on the chute bed as a function of $Fr_{steady}$; and (c, d) Centroid frequency of the experimental impact pressures generated on the cylinder and the chute bed, respectively. Gray dots represent data for the single-cylinder configuration (CS-S) from Chen et al. (2021).

## 4. Discussion

### 4.1. Effects of structural spacing on GSWs

#### 4.1.1. Geometric characteristics

The runup height ($D_{runup}$) of granular flows shows a rising trend as the dimensionless spacing ($D^*$) between the two cylinders decreases. This is due to the partial blockage caused by the dual-cylinder structure (CS-D), which constrains the flow path of the incoming granular flow. As the spacing between cylinders narrows, the channel width between the two cylinders available for flowing particles becomes increasingly restricted, intensifying particle interactions. Friction and particle interactions lead to congestion, making it more challenging for particles to pass through the gaps between cylinders, thereby resulting in higher runup heights. In comparison, granular flow experiments in the CS-S configuration (Chen et al., 2021) shows relative lower runup heights than those observed for CS-D when $D^*$ was further reduced from 1 to 0.67. This difference is likely due to the larger effective cross-sectional area available for granular flow in the single-cylinder set-up.

The dimensionless runup height ($D^*_{runup}$) increases approximately linearly with increasing steady-state Froude number ($Fr_{steady}$), as shown in Fig. 8. Comparisons with predictions from the hydraulic jump model reveal that the model systematically overpredicts the measured runup heights. The hydraulic jump model (see Eq. (3)), in particular, predicts higher runup heights compared to the experimental data and the simulated data. This is because the cylinders act both as obstructions and splitters: during the impact process, particles tend to divert around the cylinder, which limits the conversion of kinetic energy into gravitational potential energy. Consequently, the experimentally measured runup heights are lower than those predicted by models originally formulated for granular flow impacting on a planar wall. Our data show that the runup height of the granular flow correlates linearly with $Fr_{steady}$. Based on our laboratory experiments and DEM simulations, we derived an empirical relationship for granular flow runup on cylinders with varying spacings:

$$D^*_{runup} = 1.5Fr^{0.74}_{steady} \tag{17}$$

The dimensionless standoff distance ($D^*_{standoff}$) of GSWs increases as the cylinder spacing ($D^*$) decreases (Fig. 8b). This is likely due to the enhanced interactions between the two GSWs as the spacing between adjacent cylinders narrows. Previous experiments on granular flows past wedge-shaped obstacles (Jaiswal et al., 2023) showed that reducing the gap between two wedges causes individual shock waves to merge into a single, larger shock wave that envelopes both wedges. A similar mechanism operates for cylindrical structures. Subsurface upstream regions containing static or slowly moving particles develop, effectively altering the shape of the shock zone and pushing the granular shock front

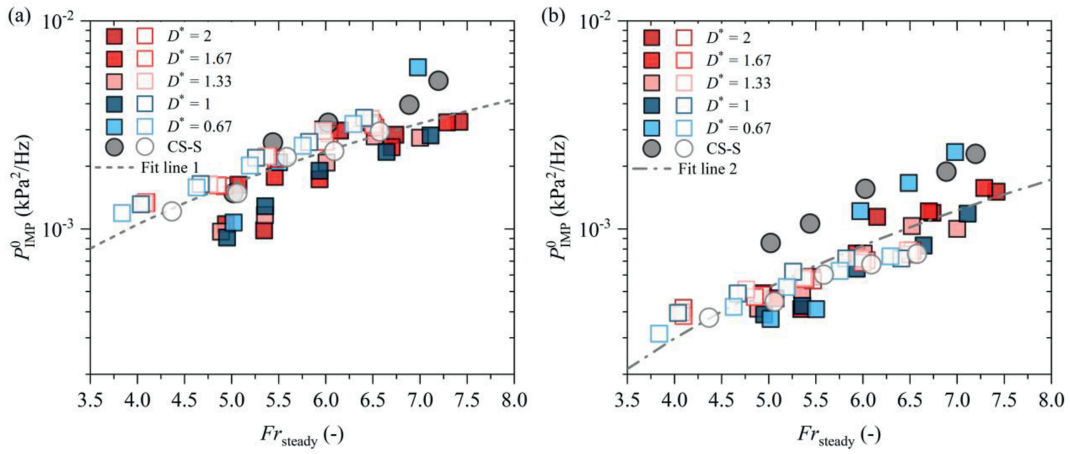


**Fig. 12.** Low-frequency power spectral density (PSD; $P^0_{IMP}$) of impact pressures generated on (a) the cylinder and (b) the chute bed, respectively, as a function of the steady-state Froude number ($Fr_{steady}$). The fitted relationships are: $y = 6.6 \times 10^{-5}\, x^{2.0}$ ($R^2 = 0.62$) (fit line 1) and $y = 8.9 \times 10^{-6}\, x^{2.5}$ ($R^2 = 0.62$) (fit line 2).

further upstream. Additionally, we also observed that $D^*_{standoff}$ decreases with increasing $Fr_{steady}$. When $Fr_{steady}$ reaches 6, both the experimental and DEM results indicate that $D^*_{standoff}$ is approximately one-fourth of the cylinder diameter, consistent with previous observations (Cui and Gray, 2013; Chen et al., 2021). Furthermore, the experimental and numerical results exceed the predictions from theoretical models (Forbes and Schwartz, 1981). This discrepancy likely reflects the influence of particle size within the GSW region: as $D^*_{standoff}$ decreases, force chains may form among particles at the steady state, making the granular assembly increasingly resistant to further compression and altering the effective propagation of the shock front.

Fig. 8c illustrates the correlation between tan$\beta$ (where $\beta$ is the net acceleration angle) and the dimensionless pinch-off distance ($D^*_{pinch-off}$) of the particle vacuum region downstream of the cylinders. The results indicate that $D^*_{pinch-off}$ increases nonlinearly with tan$\beta$, as steeper slopes accelerate the granular flow and diminish the weakening pressure gradients that drive closure of the particle vacuum. Conversely, Cui and Gray (2013) observed that $D^*_{pinch-off}$ approaches zero as tan$\beta$ tends to zero, implying that the particle vacuum nearly closes just behind the cylinder under very low slope conditions. This behavior, illustrated by the gray dots in Fig. 8c, lies outside the parameter range covered by our experiments.

Comparisons between single-cylinder (CS-S) and dual-cylinder (CS-D) configurations reveal that $D^*_{pinch-off}$ is larger for the CS-S configuration than for the CS-D configuration. Under the CS-D conditions, $D^*_{pinch-off}$ is highly sensitive to the cylinder spacing $D^*$). Fig. 8c indicates that, when $D^* = 2$, the interaction between the two GSWs is relatively weak, and the particle vacuum length is almost unaffected by the wakes from the opposite side. As $D^*$ decreases to 0.67, stronger interactions between the shock waves disturb the particle vacuum shape, leading to earlier closure of the particle-free zone and a marked reduction in $D^*_{pinch-off}$. DEM simulations reproduce this dependency and confirm that $D^*_{pinch-off}$ depends on the cylinder spacing $D^*$.

For the CS-S configuration, $D^*_{pinch-off}$ establishes the upper limit of the particle vacuum region length, following a power-law relationship: $y = 40.2x^{1.48}$ ($R^2 = 0.99$, see red dashed line in Fig. 8c). In multi-structural flow fields, as the spacing between cylinders increases, the inter-wake interactions weaken and $D^*_{pinch-off}$ for CS-D approaches the CS-S upper-limit curve. The critical spacing ($D^*_c$) at which this transition becomes complete remains undetermined, as the critical $D^*_c$ may be influenced by the Froude number and material properties of the particles. However, our data suggest that $D^*_c > 2$, though only marginally, as $D^*_{pinch-off}$ values for $D^* = 2$ already converge toward those of the CS-S configuration.

The data also showed that $D^*_{pinch-off}$ decreases significantly with decreasing spacing $D^*$. In this study, the value of $D^*_{pinch-off}$ for $D^* = 0.67$ establishes the lower limit of the particle vacuum region length, which follows the power-law relationship between $D^*_{pinch-off}$ and tan$\beta$ as $y = 25.5x^{1.61}$ ($R^2 = 0.93$; blue dashed line in Fig. 8c). Further reductions in spacing $D^*$ are predicted to shorten the particle vacuum region, although $D^*_{pinch-off}$ will not vanish entirely. The gray-shaded region in Fig. 8c represents the range of observed $D^*_{pinch-off}$ values in this study, indicating predictability under varying tan$\beta$. This power-law relationship illustrates that the extent of the granular vacuum region is strongly influenced by the net acceleration angle of the granular flow (tan$\beta$). As tan$\beta$ increases, particles acquire greater downslope momentum, resulting in longer-lasting particle vacuum zones behind obstacles. These vacuum regions are critical for assessing the protective performance of barrier systems. Furthermore, by quantifying how this relationship varies with obstacle spacing $D^*$, we define an envelope of predictable vacuum region lengths (gray shaded area in Fig. 8c), which can inform the optimal design and arrangement of protective structures to maximize shielding efficiency. These findings may provide practical insights into the design of the protective structures by offering empirical guidelines for estimating protected zones based on slope geometry and structural layout (Kattel et al., 2018).

#### 4.1.2. Turning parameter

Fig. 13 presents the relationship between the turning parameter ($\chi$) and the classic Froude number $Fr$, illustrating the characteristics of granular flow and the effect of cylinder spacing ($D$*) on $\chi$. In Fig. 13, we turn to use the classical $Fr$ to better compare our data with other models or data. The behavior of granular flow is determined by the collective motion of numerous discrete

particles, which exhibit both fluid-like and discrete medium characteristics. Our observations indicate that the value of $\chi$ tends to converge with increasing *Fr*, approaching around 0.5. Under the CS-D configuration with $D^* = 0.67$, $\chi$ values are significantly higher than those observed for larger spacing distances. This might be attributed to the smaller ratio ($k$) of tangential to normal stress, as defined in Eq. (5), which is influenced by fluctuations in the granular flow impact pressures.

### 4.2. Impact pressures in the GSW region

#### 4.2.1. Impulses, centroid frequency, and PSD

The number of impulses $N_{\text{impulse}}$ and the centroid frequency $f_{\text{centroid}}$ of the fluctuating pressures from experiments show a slight decreasing trend with increasing steady-state Froude number $Fr_{\text{steady}}$ (Fig. 11). This is likely related to the formation of granular force chains in the shock-affected region upstream of the cylinders under the steady-state flow conditions, which reduces the particle impact rate on the pressure sensors, thereby decreasing $N_{\text{impulse}}$ and $f_{\text{centroid}}$. The cylinder spacing ($D^*$) has a negative influence on $N_{\text{impulse}}$, although its effect on $f_{\text{centroid}}$ differs. This is because $N_{\text{impulse}}$ is calculated as a count of the number of effective pressure amplitudes for an entire impact process, whereas $f_{\text{centroid}}$ primarily characterizes the frequency content of the intense impact phase. A reduction in $D^*$ may shorten the overall impact duration, reducing $N_{\text{impulse}}$, whereas $f_{\text{centroid}}$ is more sensitive to the instantaneous particle collision dynamics of the intense impact process. The changes in $N_{\text{impulse}}$ and $f_{\text{centroid}}$ thus reflect the influence of structural spacing on impact dynamics within the granular shock region.

The low-frequency PSD ($P^0_{\text{IMP}}$) of the granular impact pressures demonstrates a power-law correlation with $Fr_{\text{steady}}$, which indicates an increasing impact energy with rising flow intensity. We found that $P^0_{\text{IMP}}$ for the impact pressures on the cylinder surface is significantly higher (ca. three times) than that on the chute bed. This suggests that the impact energy transfer in the granular shock region is predominantly oriented along the flow direction rather than perpendicular to the bed. Furthermore, given the same flow condition, $P^0_{\text{IMP}}$ is greater for the single-cylinder configuration (CS-S) than in the dual-cylinder configuration (CS-D) with varying spacing (Fig. 12). This might be due to the fact that part of the impact energy is dissipated due to interactions between the GSWs.

#### 4.2.2. Impact pressure coefficient

The dimensionless impact pressure ($\alpha$), also known as the impact pressure coefficient, is typically estimated through laboratory experiments and field observations, and is expressed as a power-law function of *Fr*: $\alpha = IMP/(\rho u_1^2) = a(Fr)^b$. Previous studies using data from flume experiments and field investigations have proposed various empirical models for $\alpha$ (Hübl et al., 2009; Scheidl et al., 2013; Cui et al., 2015; Wang et al., 2018a, 2018b). In this study, the mean impact pressure generated by the granular flow body ($IMP_{\text{mean-body,C}}$) is used to examine the relationship between $\alpha$ and *Fr* (Fig. 13b). The results are compared with existing models and experimental datasets from previous research. The results reveal that $\alpha$ decreases nonlinearly with increasing *Fr* and shows relatively less sensitivity to changes in cylinder spacing ($D^*$). This decreasing trend may reflect the transition from dense, contact-dominated flow regimes at lower velocities to more dilute, inertia-dominated regimes at higher velocities. In such high-*Fr* flows, particles tend to bypass the obstacle with less effective momentum transfer, leading to reduced impact pressure relative to the dynamic pressure baseline. Based on laboratory experiments and DEM simulations, we propose the following empirical relationship between $\alpha$ and *Fr* for granular flow impacts on cylindrical structures (solid red line in Fig. 13b):

$$\alpha = 1.04Fr^{-0.6} \tag{18}$$

At low Froude numbers, $\alpha$ values for granular flows are smaller than those reported for debris flow data from field investigations and flume experiments, most likely due to differences in flow rheology and phase composition. However, at high *Fr* ($Fr > 6$), $\alpha$ values for granular flows converge toward those for debris flows. One possible explanation is that the role of the fluid phase in the impact process varies under different Froude numbers. Debris flows are typically considered a mixture of solid and fluid phases, or further divided into three phases: fluid phase (a mixture of water and very fine particles), fine solid phase (clay, silt, and sand), and solid phase (gravels, pebbles, and boulders) (Pudasaini and Mergili, 2019). The relative contributions of these phases to the impact dynamics vary under different conditions, adding complexity to impact force estimation in debris flows. For "viscous debris flow", where the viscosity of the fluid phase dominates, the resulting *Fr* is typically lower, leading to reduced inertial forces (Wang et al., 2018b). In contrast, dry granular flows, which lack a fluid phase, exhibit smaller values of the impact pressure

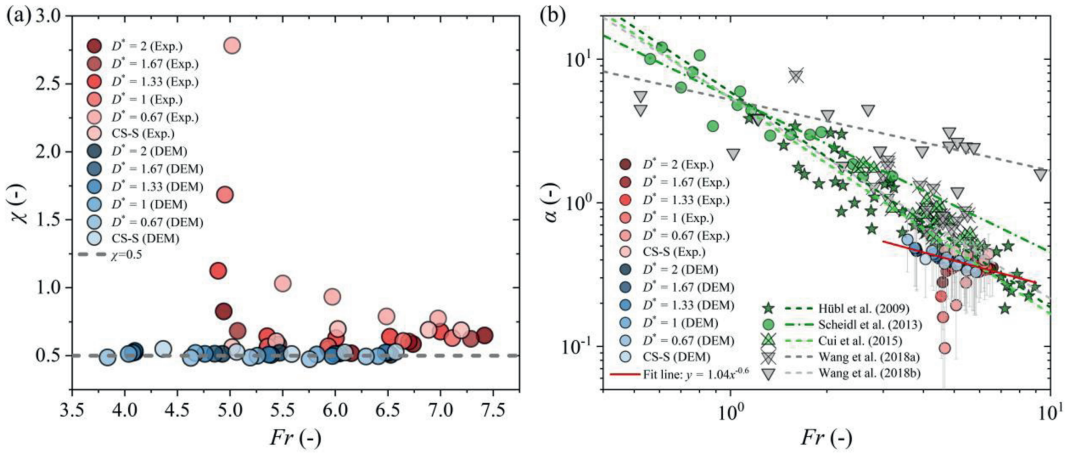


**Fig. 13.** The turning parameter ($\chi$) and the impact pressure coefficient ($\alpha$): (a) $\chi$ as a function of classic Froude number *Fr*; and (b) $\alpha$, determined by impact pressures generated by granular flow body, as a function of *Fr*.

coefficient ($\alpha$). Conversely, in a "diluted debris flow", where the viscous force of the fluid phase exerts minimal influence, higher *Fr* values are observed under similar slope conditions. In such cases, inertial forces dominate the impact process, and the impact pressures are primarily governed by the coarse solid particles, with minimal contribution from the fluid phase.

Although the present study provides some new insights into the dynamics of granular flow impacts on cylinders, we acknowledge that the experimental conditions differ from those in natural granular flow hazards, particularly in terms of GSD, flow scale, and material complexity. Throughout the flow process, we did not observe significant particle segregation along the slope or over time, as confirmed by the visual distribution of colored beads. Minor differences at the flow front, likely caused by saltating particles, were confined to the leading edge and did not affect the steady-state measurements on which our analysis is based. Nevertheless, we recognize that segregation effects may become more significant in flows with broader size ranges or more complex boundary conditions, and this aspect warrants further investigation in future studies.

Despite these limitations, the dimensionless relationships established here show good comparability with existing studies and offer preliminary guidance for the design of protective structures, particularly in optimizing obstacle spacing to regulate shock wave interactions and energy dissipation. Further quantitative characterization of GSWs, including shock front evolution, particle-scale velocity fields, and energy transfer mechanisms, will be essential for developing more applicable and predictive models. Future work will therefore focus on field-scale validation, parameter calibration, and large-scale modeling, and refined analyses of granular shock dynamics using high-speed imaging, dynamic force measurements, and advanced DEM post-processing. These efforts aim to improve the quantitative description and the theoretical framework of GSWs, thereby contributing to granular-flow hazard mitigation.

## 5. Conclusions

This study systematically investigated the dynamics of GSWs interacting with cylindrical obstacles of varying spacings through laboratory-scale experiments and DEM simulations. Key geometry features, namely runup height, standoff distance, and pinch-off distance of particle vacuum region, were quantitatively analyzed.

The results demonstrate that the runup height increases with the Froude number but decreases as the cylinder spacing widens. The standoff distance decreases, while the pinch-off distance increases with increasing cylinder spacing, indicating that strong granular interactions significantly modify granular flow morphology within the shock region.

Impact pressures generated by granular flow increase linearly with the Froude number, while the dimensionless pressure coefficient decreases nonlinearly and converges toward established debris flow models at high Froude numbers. Spectral analysis shows that the PSD of granular impact pressures follows a power-law correlation with increasing steady-state Froude number. Pressure PSD values are significantly higher on the cylinder surface than on the chute bed and are lower for dual-cylinder configurations compared to single-cylinder cases, reflecting enhanced energy dissipation due to interactions between GSWs. These findings may improve our understanding of GSW dynamics and provide useful insights for designing protective structures to mitigate granular flow hazards.

## CRediT authorship contribution statement

**Zheng Chen:** Writing – review & editing, Writing – original draft, Visualization, Validation, Project administration, Methodology, Investigation, Funding acquisition, Formal analysis, Data curation. **Jian Wang:** Visualization, Software, Formal analysis. **Dongpo Wang:** Supervision. **Siming He:** Writing – review & editing, Supervision, Software, Conceptualization.

## Data availability statement

Datasets for this research are available upon request to the readers.

Notations

| | |
|---|---|
| $\bar{A_Z}$ | Amplitude obtained by a fast Fourier transform of the impact pressures (kPa/Hz) |
| $\overline{u}$ | Depth-averaged velocity in the *x*-direction (m/s) |
| $D$ | Spacing distance between cylindrical obstacles (m) |
| $D^*$ | Dimensionless spacing distance between cylindrical obstacles |
| $D^*_{\text{pinch-off}}$ | Dimensionless pinch-off distance |
| $D^*_{\text{runup}}$ | Dimensionless runup height |
| $D^*_{\text{standoff}}$ | Dimensionless standoff distance |
| $D_{\text{pinch-off}}$ | Pinch-off distance (m) |
| $D_{\text{runup}}$ | Runup height (m) |
| $D_{\text{standoff}}$ | Standoff distance (m) |
| $e$ | Restitution coefficient |
| $E^*$ | Equivalent Young's modulus of particles (Pa) |
| $E_{\text{i}}$ | Elastic modulus of particles *i* (Pa) |
| $f_{\text{centroid}}$ | Centroid frequency (Hz) |
| FFT | Fast Fourier transform |
| $F_{\text{n}}$ | Normal force (N) |
| $F^{\text{d}}_{\text{n}}$ | Normal damping force (N) |
| $Fr$ | Classic Froude number |
| $Fr_{\text{front}}$ | Front flow Froude number |
| $Fr_{\text{steady}}$ | Steady-state Froude number |
| $F^{\text{d}}_{\text{t}}$ | Tangential damping force (N) |
| $g$ | Gravity acceleration (m/s$^2$) |
| $G^*$ | Equivalent shear modulus (Pa) |
| $G_{\text{i}}$ | Shear modulus of particles *i* (Pa) |
| GSD | Grain size distribution |

(*continued*)

| | |
|---|---|
| GSW | Granular shock wave |
| $h_1$ | Flow depth of an incoming flow (m) |
| $h_2$ | Runup height (m) |
| $IMP$ | Dynamic impact pressure (kPa) |
| $IMP_{\text{mean\_all,B}}$ | Mean impact pressure caused by granular flow on chute bed (kPa) |
| $IMP_{\text{mean\_all,C}}$ | Mean impact pressure caused by granular flow on a cylinder surface (kPa) |
| $IMP_{\text{mean\_body,B}}$ | Mean impact pressure caused by granular flow body on chute bed (kPa) |
| $IMP_{\text{mean\_body,C}}$ | Mean impact pressure caused by the granular flow body on a cylinder surface (kPa) |
| $IMP_{\text{mean\_head,B}}$ | Mean impact pressure caused by granular flow head on chute bed (kPa) |
| $IMP_{\text{mean\_head,C}}$ | Mean impact pressure caused by granular flow head on a cylinder surface (kPa) |
| $IMP_{\text{peak\_head,B}}$ | Peak impact pressure caused by granular flow head on chute bed (kPa) |
| $IMP_{\text{peak\_head,C}}$ | Peak impact pressure caused by granular flow head on a cylinder surface (kPa) |
| $K$ | Coefficient related to the shape of the jump |
| $k$ | Earth pressure coefficient |
| $L$ | Length of granular jump region (m) |
| $m_i$ | Mass of particle $i$ (kg) |
| $P^0_{\text{IMP}}$ | Low-frequency power spectral density of the impact pressures ($kPa^2$/Hz) |
| $R^*$ | Equivalent radius of particles (m) |
| $R_c$ | Radius of cylinder (m) |
| $R_i$ | Radius of particles $i$ (m) |
| $R_p$ | Distance from the contact point to the center of mass (m) |
| $S_n$ | Normal stiffness (N/m) |
| $S_t$ | Tangential stiffness (N/m) |
| $u_1$ | Incoming flow velocity (m/s) |
| $v_n^{rel}$ | Normal component of the relative velocity (m/s) |
| $v_t^{rel}$ | Tangential component of the relative velocity (m/s) |
| $\alpha$ | Impact pressure coefficient |
| $\beta$ | Velocity profile shape coefficient of the granular flow |
| $\delta_t$ | Tangential overlap between particles (m) |
| $\theta$ | Slope angle (°) |
| $\upsilon$ | Poisson's ratio of the particle |
| $\chi$ | Tuning parameter linking the traditional hydraulic jump to the granular jump |
| $\omega_i$ | Unit angular velocity vector (rad/s) |
| $\delta$ | Dynamic friction angle (°) |
| $\mu_r$ | Rolling friction coefficient |
| $\mu_s$ | Static friction coefficient |
| $\mu_b$ | Basal friction coefficient |
| $\phi$ | Effective basal friction angle (°) |

## Declaration of competing interest

The authors declare that they have no known competing financial interests or personal relationships that could have appeared to influence the work reported in this paper.

## Acknowledgments

This study was supported by the National Natural Science Foundation of China (NSFC) (Grant No. 42307254), the Sichuan Science and Technology Program (Grant No. 2024NSFSC0861), and the State Key Laboratory of Geohazard Prevention and Geo-environment Protection Independent Research Project (Grant No. SKLGP2022Z024). The first author acknowledges Dr. Yi Zhang from the Institute of Mountain Hazards and Environment, Chinese Academy of Sciences, for his support with the laboratory chute experiments conducted in the summer of 2019. The first author also thanks Prof. Shiva P. Pudasaini from the Technical University of Munich for his suggestions on an early version of this manuscript.

## Appendixces

Appendices A–D to this article can be found online at https://doi.org/10.1016/j.jrmge.2025.10.034.

## References

Albaba, A., Lambert, S., Faug, T., 2017. Dry granular avalanche impact force on a rigid wall of semi-infinite height. EPJ Web Conf. 140, 03054.

Armanini, A., 2007. On the dynamic impact of debris flows. In: Armanini, A., Michiue, M. (Eds.), Recent Developments on Debris Flows. Springer, Berlin, Heidelberg, pp. 208–226. German.

Armanini, A., Larcher, M., Odorizzi, M., 2011. Dynamic impact of a debris flow against a vertical wall. Ital. J. Eng. Geol. Environ. 1 (1), 1041–1049.

Bi, Y., Du, Y., He, S., Sun, X., Wang, D., Li, X., Liang, H., Wu, Y., 2018. Numerical analysis of effect of baffle configuration on impact force exerted from rock avalanches. Landslides 15 (5), 1029–1043.

Boudet, J.F., Amarouchene, Y., Bonnier, B., Kellay, H., 2007. The granular jump. J. Fluid Mech. 572, 413–431.

Boudet, J.F., Kellay, H., 2010. Drag coefficient for a circular obstacle in a quasi-two-dimensional dilute supersonic granular flow. Phys. Rev. Lett. 105 (10), 104501.

Brennen, C.E., Sieck, K., Paslaski, J., 1983. Hydraulic jumps in granular material flow. Powder Technol. 35 (1), 31–37.

Bugnion, L., McArdell, B.W., Bartelt, P., Wendeler, C., 2012. Measurements of hill-slope debris flow impact pressure on obstacles. Landslides 9 (2), 179–187.

Calvetti, F., Di Prisco, C.G., Vairaktaris, E., 2017. DEM assessment of impact forces of dry granular masses on rigid barriers. Acta Geotech. 12 (1), 129–144.

Chen, H., Tang, H., Xian, X., Zhang, Y., 2010. Experimental model of debris flow impact features. J. Chongqing Univ. 33 (5), 114–119 (in Chinese).

Chen, Z., He, S., Shen, W., Wang, D., 2022. Effects of defense-structure system for bridge piers on two-phase debris flow wakes. Acta Geotech. 17 (5), 1645–1665.

Chen, Z., Rickenmann, D., Zhang, Y., He, S., 2021. Effects of obstacle's curvature on shock dynamics of gravity-driven granular flows impacting a circular cylinder. Eng. Geol. 293, 106343.

Chen, Z., Wang, J., Luo, M., Wang, D., He, S., 2025. An analytical model of particle impact rate in partially dense inclined granular flow driven by gravity. Earth Space Sci. 12 (8) e2024EA003655.

Choi, C.E., Ng, C.W.W., Song, D., Kwan, J.H.S., Shiu, H.Y.K., Ho, K.K.S., Koo, R.C.H., 2014. Flume investigation of landslide debris–resisting baffles. Can. Geotech. J. 51 (5), 540–553.

Cui, P., Zeng, C., Lei, Y., 2015. Experimental analysis on the impact force of viscous debris flow. Earth Surf. Process. Landf. 40 (12), 1644–1655.

Cui, X., Gray, J.M.N.T., 2013. Gravity-driven granular free-surface flow around a circular cylinder. J. Fluid Mech. 720, 314–337.

Cui, X., Harris, M., Howarth, M., Zealey, D., Brown, R., Shepherd, J., 2022. Granular flow around a cylindrical obstacle in an inclined chute. Phys. Fluids 34 (9), 093308.

Dai, Z., Huang, Y., Cheng, H., Xu, Q., 2017. SPH model for fluid–structure interaction and its application to debris flow impact estimation. Landslides 14 (3), 917–928.
Farin, M., Mangeney, A., De Rosny, J., Toussaint, R., Trinh, P.T., 2018. Link between the dynamics of granular flows and the generated seismic signal: insights from laboratory experiments. J. Geophys. Res.: Earth Surf. 123 (6), 1407–1429.
Farin, M., Mangeney, A., de Rosny, J., Toussaint, R., Trinh, P.T., 2019. Relations between the characteristics of granular column collapses and resultant high-frequency seismic signals. J. Geophys. Res.: Earth Surf. 124 (12), 2987–3021.
Faug, T., 2015a. Depth-averaged analytic solutions for free-surface granular flows impacting rigid walls down inclines. Phys. Rev. E 92 (6), 062310.
Faug, T., 2015b. Macroscopic force experienced by extended objects in granular flows over a very broad froude-number range. Eur. Phys. J. E 38 (5), 34.
Faug, T., Gauer, P., Lied, K., Naaim, M., 2008. Overrun length of avalanches overtopping catching dams: cross-comparison of small-scale laboratory experiments and observations from full-scale avalanches. J. Geophys. Res.: Earth Surf. 113, F03009.
Fischer, L., Purves, R.S., Huggel, C., Noetzli, J., Haeberli, W., 2012. On the influence of topographic, geological and cryospheric factors on rock avalanches and rockfalls in high-mountain areas. Nat. Hazards Earth Syst. Sci. 12 (1), 241–254.
Forbes, L.K., Schwartz, L.W., 1981. Supercritical flow past blunt bodies in shallow water. Z. fur Angew. Math. Phys. 32 (3), 314–328.
George, D.L., Iverson, R.M., 2014. A depth-averaged debris-flow model that includes the effects of evolving dilatancy. II. Numerical predictions and experimental tests. Proc. R. Soc. A: Math. Phys. Eng. Sci. 470 (2170), 20130820.
Gray, J.M.N.T., Cui, X., 2007. Weak, strong and detached oblique shocks in gravity-driven granular free-surface flows. J. Fluid Mech. 579, 113–136.
Gray, J.M.N.T., Tai, Y.C., Noelle, S., 2003. Shock waves, dead zones and particle-free regions in rapid granular free-surface flows. J. Fluid Mech. 491, 161–181.
Heil, P., Rericha, E.C., Goldman, D.I., Swinney, H.L., 2004. Mach cone in a shallow granular fluid. Phys. Rev. E 70 (6), 060301.
Hu, K., Wei, F., Li, Y., 2011. Real-time measurement and preliminary analysis of debris-flow impact force at Jiangjia Ravine, China. Earth Surf. Process. Landf. 36 (9), 1268–1278.
Hübl, J., Suda, J., Proske, D., Kaitna, R., Scheidl, C., 2009. Debris flow impact estimation. In: Proceedings of the 11th International Symposium on Water Management and Hydraulic Engineering, pp. 137–148. Ohrid, Macedonia.
Hungr, O., Morgan, G.C., Kellerhals, R., 1984. Quantitative analysis of debris torrent hazards for design of remedial measures. Can. Geotech. J. 21 (4), 663–677.
Iverson, R.M., George, D.L., Logan, M., 2016. Debris flow runup on vertical barriers and adverse slopes. J. Geophys. Res.: Earth Surf. 121 (12), 2333–2357.
Johnson, C.G., Gray, J.M.N.T., 2011. Granular jets and hydraulic jumps on an inclined plane. J. Fluid Mech. 675, 87–116.
Jibson, R.W., Harp, E.L., Schulz, W., Keefer, D.K., 2006. Large rock avalanches triggered by the M 7.9 Denali Fault, Alaska, earthquake of 3 November 2002. Eng. Geol. 83, 144–160.
Jakob, M., Stein, D., Ulmi, M., 2012. Vulnerability of buildings to debris flow impact. Nat. Hazards 60 (2), 241–261.
Jaiswal, Y., Khan, A., Kumar, R., Kumar, S., 2023. Shocked confined-granular flow over obstacles. J. Fluid Mech. 960, A21.
Kafle, J., Kattel, P., Mergili, M., Fischer, J.T., Pudasaini, S.P., 2019. Dynamic response of submarine obstacles to two-phase landslide and tsunami impact on reservoirs. Acta Mech. 230 (9), 3143–3169.
Kang, H.S., Kim, Y.T., 2016. The physical vulnerability of different types of building structure to debris flow events. Nat. Hazards 80 (3), 1475–1493.
Kattel, P., Kafle, J., Fischer, J.T., Mergili, M., Tuladhar, B.M., Pudasaini, S.P., 2018. Interaction of two-phase debris flow with obstacles. Eng. Geol. 242, 197–217.
Khan, A., Verma, S., Hankare, P., Kumar, R., Kumar, S., 2020. Shock–shock interactions in granular flows. J. Fluid Mech. 884, R4.
Kwan, J.S., Chan, S.L., Cheuk, J.C., Koo, R.C.H., 2014. A case study on an open hillside landslide impacting on a flexible rockfall barrier at Jordan Valley, Hong Kong. Landslides 11, 1037–1050.
Liang, H., He, S., Chen, Z., Liu, W., 2019. Modified two-phase dilatancy SPH model for saturated sand column collapse simulations. Eng. Geol. 260, 105219.
Mindlin, R.D., 1949. Compliance of elastic bodies in contact. J. Appl. Mech. 16 (3), 259–268.
Mindlin, R.D., Deresiewicz, H., 1953. Elastic spheres in contact under varying oblique forces. J. Appl. Mech. 20 (3), 327–344.
Moriguchi, S., Borja, R.I., Yashima, A., Sawada, K., 2009. Estimating the impact force generated by granular flow on a rigid obstruction. Acta Geotech. 4 (1), 57–71.
Ng, C.W.W., Song, D., Choi, C.E., Liu, L.H.D., Kwan, J.S.H., Koo, R.C.H., Pun, W.K., 2017. Impact mechanisms of granular and viscous flows on rigid and flexible barriers. Can. Geotech. J. 54 (2), 188–206.
Pudasaini, S.P., 2011. Some exact solutions for debris and avalanche flows. Phys. Fluids 23 (4), 043301.
Pudasaini, S.P., 2024. Extended landslide velocity and analytical drag. Eur. Phys. J. Plus 139 (2), 131.
Pudasaini, S.P., Hutter, K., Hsiau, S.S., Tai, S.C., Wang, Y., Katzenbach, R., 2007. Rapid flow of dry granular materials down inclined chutes impinging on rigid walls. Phys. Fluids 19 (5), 053302.
Pudasaini, S.P., Krautblatter, M., 2022. The landslide velocity. ESurf 10 (2), 165–189.
Pudasaini, S.P., Kröner, C., 2008. Shock waves in rapid flows of dense granular materials: theoretical predictions and experimental results. Phys. Rev. E. 78 (4), 041308.
Pudasaini, S.P., Mergili, M., 2019. A multi-phase mass flow model. J. Geophys. Res.: Earth Surf. 124 (12), 2920–2942.
Pudasaini, S.P., Tiwari, C.N., Dangol, B.R., Kafle, J., Pokhrel, P.R., Kattel, P., 2024. Impact pressure coefficient and object mobilization length in mass flows. Phys. Fluids 36 (8), 083312.
Pudasaini, S.P., Wang, Y., Hutter, K., 2005. Modelling debris flows down general channels. Nat. Hazards Earth Syst. Sci. 5 (6), 799–819.
Rickenmann, D., Turowski, J.M., Fritschi, B., et al., 2014. Bedload transport measurements with impact plate geophones: comparison of sensor calibration in different gravel-bed streams. Earth. Surf. Process. Landf. 39 (7), 928–942.
Sakaguchi, H., Ozaki, E., Igarashi, T., 1993. Plugging of the flow of granular materials during the discharge from a silo. Int. J. Mod. Phys. B 7, 1949–1963.
Savage, S.B., 1979. Gravity flow of cohesionless granular materials in chutes and channels. J. Fluid Mech. 92 (1), 53–96.
Savage, S.B., Hutter, K., 1989. The motion of a finite mass of granular material down a rough incline. J. Fluid Mech. 199, 177–215.
Scheidl, C., Chiari, M., Kaitna, R., Müllegger, M., Krawtschuk, A., Zimmermann, T., Proske, D., 2013. Analysing debris-flow impact models, based on a small scale modelling approach. Surv. Geophys. 34 (1), 121–140.
Scotton, P., Deganutti, A.M., 1997. Phreatic line and dynamic impact in laboratory debris flow experiments. In: Debris-Flow Hazards Mitigation – Mechanics, Prediction, and Assessment. Millpress Science, Rotterdam, Netherlands, pp. 777–786.
Shen, W., Wang, D., Qu, H., Li, T., 2019. The effect of check dams on the dynamic and bed entrainment processes of debris flows. Landslides 16 (11), 2201–2217.
Shieh, C.L., Chia-Hsien, T.I.N.G., Hung-Wen, P.A.N., 2008. Impulsive force of debris flow on a curved dam. Int. J. Sediment Res. 23 (2), 149–158.
Song, D., Choi, C.E., Ng, C.W.W., Zhou, G.G.D., 2018. Geophysical flows impacting a flexible barrier: effects of solid–fluid interaction. Landslides 15 (1), 99–110.
Tai, Y.C., Gray, J.M.N.T., Hutter, K., Noelle, S., 2001. Flow of dense avalanches past obstructions. Ann. Glaciol. 32, 281–284.
Thielicke, W., Sonntag, R., 2021. Particle image velocimetry for MATLAB: Accuracy and enhanced algorithms in PIVlab. J. Open Res. Softw. 9 (1), 1–14.
Tiberghien, D., Laigle, D., Naaim, M., Thibert, E., Ousset, F., 2007. Experimental investigations of interaction between mudflow and an obstacle. In: Debris-Flow Hazards Mitigation – Mechanics, Prediction and Assessment. Millpress Science, Rotterdam, Netherlands, pp. 681–687.
Tregaskis, C., Johnson, C.G., Cui, X., Gray, J.M.N.T., 2022. Subcritical and supercritical granular flow around an obstacle on a rough inclined plane. J. Fluid Mech. 933, A25.
Vagnon, F., Segalini, A., 2016. Debris flow impact estimation on a rigid barrier. Nat. Hazards Earth Syst. Sci. 16 (7), 1691–1697.
Wang, Y., Liu, X., Yao, C., Li, Y., Liu, S., Zhang, X., 2018a. Finite release of debris flows around round and square piers. J. Hydraul. Eng. 144 (12), 06018015.
Wang, D., Chen, Z., He, S., Liu, Y., Tang, H., 2018b. Measuring and estimating the impact pressure of debris flows on bridge piers based on large-scale laboratory experiments. Landslides 15 (7), 1331–1345.
Wendeler, C., Volkwein, A., 2015. Laboratory tests for the optimization of mesh size for flexible debris-flow barriers. Nat. Hazards Earth Syst. Sci. 15 (12), 2597–2604.
Zanuttigh, B., Lamberti, A., 2006. Experimental analysis of the impact of dry avalanches on structures and implication for debris flows. J. Hydraul. Eng. 44 (4), 522–534.
Zhang, B., Bi, Y., Huang, Y., 2024b. Centrifuge modelling of dry granular run-out processes under deflective Coriolis condition. J. Rock Mech. Geotech. Eng. 17 (2), 1227–1239.
Zhang, B., Li, W., Pu, J., Bi, Y., Huang, Y., 2024a. Centrifuge and DEM investigation of dry granular impacts: effect of granular volume under high-speed impact conditions. Landslides 21 (6), 1439–1459.
Zhu, L., Liang, H., He, S., Liu, W., Zhang, Q., Li, G., 2020. Failure mechanism and dynamic processes of rock avalanche occurrence in Chengkun railway, China, on August 14, 2019. Landslides 17 (4), 943–957.

**Zheng Chen** received his PhD degree in Geotechnical Engineering from the University of Chinese Academy of Sciences in 2022, with substantial training and research experience at the Institute of Mountain Hazards and Environment, Chinese Academy of Sciences (2016–2022), and the Swiss Federal Research Institute WSL, Switzerland (2019–2022) during his doctoral studies. He has been an Assistant Research Fellow/Professor at the State Key Laboratory of Geohazard Prevention and Geoenvironment Protection, Chengdu University of Technology, since 2022, and presently holds a postdoctoral fellowship at WSL (ETH-domain). His research focuses on sediment transport processes and geophysical mass flows, with particular interests in (1) bedload transport monitoring with acoustic systems, (2) debris flow/flood dynamics, and (3) shock wave dynamics in granular flows.